Radon background evolution for XENONnT

Master's thesis

Westfälische Wilhelms-Universität Münster

Institut für Kernphysik

written by

Mark von Piechowski

20th January, 2023

Plagiatserklärung

Hiermit versichere ich, dass die vorliegende Arbeit über

"Radon background evolution for XENONnT"

selbstständig verfasst worden ist, dass keine anderen Quellen und Hilfsmittel als die angegebenen benutzt worden sind und dass die Stellen der Arbeit, die anderen Werken – auch elektronischen Medien – dem Wortlaut oder Sinn nach entnommen wurden, auf jeden Fall unter Angabe der Quelle als Entlehnung kenntlich gemacht worden sind.

Münster, 20. Januar 2023

Ich erkläre mich mit einem Abgleich der Arbeit mit anderen Texten zwecks Auffindung von Übereinstimmungen sowie mit einer zu diesem Zweck vorzunehmenden Speicherung der Arbeit in eine Datenbank einverstanden.

Münster, 20. Januar 2023

Contents

1 Introduction

The world of physics has not been fully understood yet. Unsolved questions are both on little scale in quantum mechanics and on large scale in astrophysics. One central mystery at the large scale are phenomena which appear with gravitational origin where the impact leads to more gravitation than the visible matter could provide. Rotational curves of galaxies [1–3] and gravitational lenses [4] show both another behavior than expected from the visible part of matter. The solution for this problem could be connected to the field of quantum mechanics where a new particle could be added interacting only gravitational and not electromagnetic, hence called dark matter. Proposed candidates for these particles are e.g. sterile neutrinos [5–7], axions [8, 9] or weakly interacting massive particles (WIMPs) [10, 11]. The direct detection of the WIMPs is one of the most promising approach for verifying the concept of dark matter. Because the thus called WIMPs only interact weak, ultra precise detectors are needed for tracking a gravitational induced collision of a WIMP. Dual-phase xenon time projection chambers (TPCs) [12] are the state-of-the-art detectors for such low signal experiment, because they profit from the high atomic mass and cross section of xenon and the spatial resolution of a TPC. For providing the best statistics the mass of xenon increased over the years [13–17], but beyond the increasing mass a decreasing background is necessary for getting the best sensitivity. Therefore, the experiments are located underground avoiding cosmic rays but still the internal background arising from the β emitter ^{214}Pb coming from the emanated ^{222}Rn is currently the biggest problem [18, 19].

The XENON collaboration runs one of the competing experiment permanently improved for the direct WIMP detection, currently named XENONnT [20]. Although the experiment is this sensitive that it could detect the double electron capture of ^{124}Xe with a half-life of $1.8 \cdot 10^{22}$y [21], the background originating from ^{222}Rn still affects the WIMP search. The emanation sources were permanently reduced by selecting specific materials [22, 23] but as the radiopurity now seems like not further increasable, a different radon reduction is taken into account via cryogenic distillation [24–26]. The ^{222}Rn activity with radiopure materials of $4.2\,\mu$Bq/kg [23] is according to the latest publication [20] during the first science run (SR0) reduced by this technique to $1.7\,\mu$Bq/kg and should further be reduced to values $< 1\,\mu$Bq/kg, which would drastically increase the WIMP sensitivity [18]. Determining the correct activity is crucial for the WIMP search to set a limit on the ^{214}Pb background.

This thesis checks the published ^{222}Rn activity and gives an alternative approach for estimating it. The method is based on a Poisson-likelihood chi-square α spectrum fit. In chapter 2 an introduction on the evidences for dark matter and the direct detection with a dual-phase xenon TPC will be given. Afterwards in chapter 3, the intrinsic backgrounds and the reduction of them are discussed. The ^{222}Rn background will be stressed out and the new cryogenic distillation for reducing it is introduced and the method of how to monitor the activity. This process will be applied in chapter 4 to estimate the rate evolution of ^{222}Rn and its decay product ^{218}Po. Therefore, own data processing cuts and corrections will be managed. Finally, the published ^{222}Rn activity is checked.

2 Dark matter and direct detection methods

The concept of dark matter was introduced because of some gravitational phenomena in astronomical dimensions which could be all explained by a deficit of visible matter with respect to the gravitational effects. The hence called missing *dark* matter could consists of unknown particles not electromagnetically interacting for which several theories fulfill the requirements for such effects. A few of the candidates for being a dark matter particle are sterile neutrinos [5–7], axions [8, 9] or weakly interacting massive particles (WIMPs) [10, 11]. Until now, only the weak gravitational effects of this matter are known.

So first of all, two of the phenomena leading to the assumption of such a theory are explained. After that, it will be shown, how the gravitational interaction can be used for directly detecting a WIMP and why the detector concept of a dual phase time projection chamber (TPC) is advantageous. As a last point of this chapter, the operation of a TPC at the XENONnT dark matter project will be presented.

2.1 Evidences for dark matter

Due to the fact that dark matter seems to interact only gravitational and the gravitation is this weak, evidences could be observed best in big structures of the universe. Most of the effects coming from additional gravity due to dark matter are not directly comprehensible and can only be verified by comparing the observations with simulations. More complex phenomena are e.g. the formation of the universe [27] or the anisotropy of the cosmic microwave background [28]. But presented here are two more understandable effects given the rotation curves [1] of galaxies and the gravitational lensing [4].

First starting with the rotation curves which show the tangential velocity of stars depending on the distance to the galactic center. An example of the M33 galaxy is shown in Figure 2.1 [2, 29] where the velocity of the stars is measured by the red or blue shift of molecular lines. As one can see, the velocity rises by rising distance from the galactic center which is in conflict with the prediction of classical mechanics. This prediction of a descent in the velocity can be seen at the luminous gas halo and the stellar disc contribution where the mass densities are known. The rising velocity is explained by an expanded dark matter halo which induces additional gravitation beyond the outer galaxy part at radius $> 8\,\mathrm{kpc}$. Even by considering the uncertainty of the velocities, the same discrepancy can be observed and explained by dark matter at many other galaxies [3].

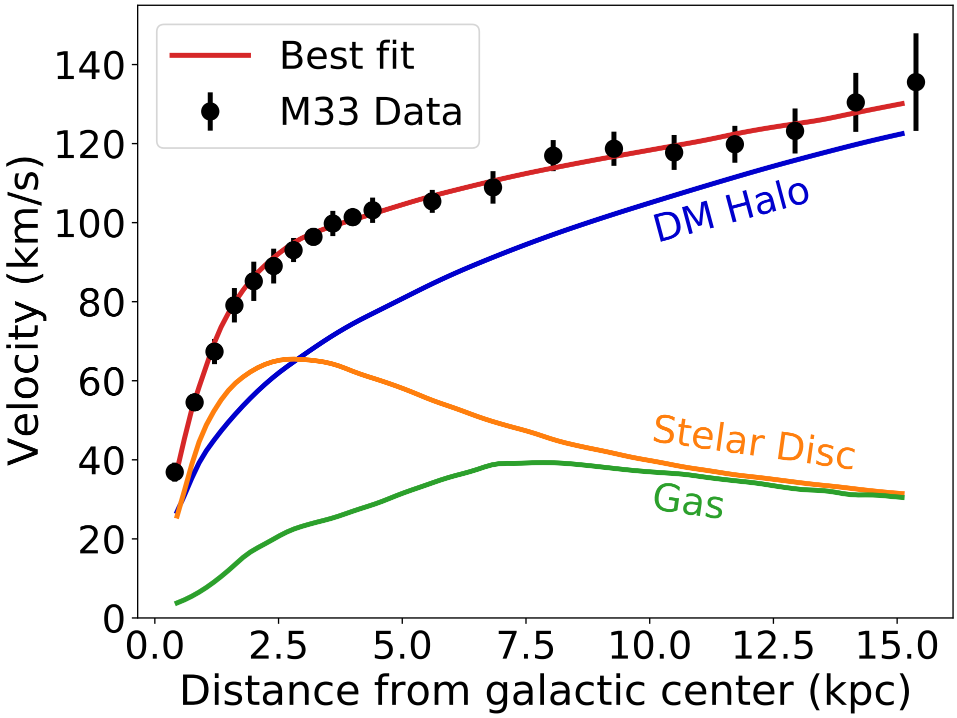

Figure 2.1: Circular velocity of stars in the M33 galaxy dependent on the distance from the galactic center. The contributing effects to the final velocity dependence of a dark matter (DM) halo, the stellar disc and gas are printed as well. One can see that the curve fits especially at $> 5.0\,\mathrm{kpc}$ only to the data because of the dark matter contribution so it is essential to the model. Figure taken from [29] with data from [2].

The other observation presented here where dark matter is introduced because of a missing luminous gravitation is the strength of gravitational lenses. As the general relativity theory predicts, masses lead to a curvature in spacetime which can be seen in galactic scales as image distortions of far galaxies. For example, galaxy clusters in the foreground lead to deflections of shining objects in the background. As a consequence, one can measure the luminous mass density of the foreground object, calculates the predicted distortions and compare it with the measured image. In particular, one differentiates between the grade of lensing in strong, weak and microlensing. Strong lensing is defined as the visibility of multiple background images. They are based on the high gravity of the foreground object which makes multiple bending paths around it possible (see red lines in Figure 2.2 [30]). But this case is unusual because most of the rays to earth propagate far from gravitational centers. The cases of less strong deflection are called weak lensing or microlensing (see white lines in Figure 2.2). Because of the smaller variations, these methods have to compare structures over time or investigate many galaxies. [4]

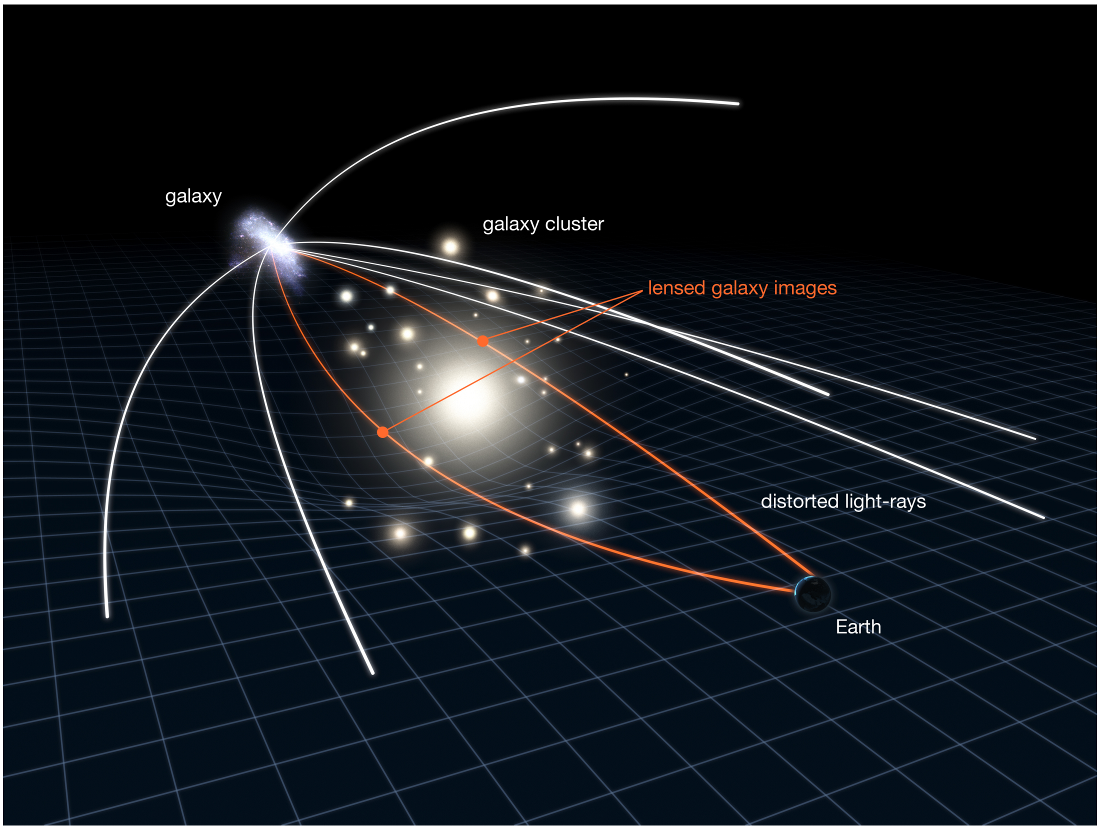

Figure 2.2: Illustration of a gravitational lens arising from a galaxy cluster. The image of the far galaxy in the background is seen deflected on earth because of the curvature in spacetime (bottom grid) of the galaxy cluster. The diffraction near the cluster center is this huge that the background image can be seen via multiple paths (strong lensing). The farther the rays are from the center the smaller is the deflection and the galaxy image can only be seen once (microlensing, weak lensing). [30]

2.2 Xenon dual phase time projection chamber

As it has become apparent in the previous section, dark matter induces only small influences in gravitation and is thus only visible in galactic dimensions. So detecting dark matter directly by a collision experiment needs high statistics and sensitivity. The latter can be reached by excluding the signal background at the best. This is possible with the detector concept of a dual phase time projection chamber (TPC) presented here. Its main advantages are the possibility to distinguish between the collision with an electron (electronic recoil, ER) or with the nucleus (nuclear recoil, NR) and to detect both scintillation and ionization light if it is filled with a liquid noble gas [12, 31].

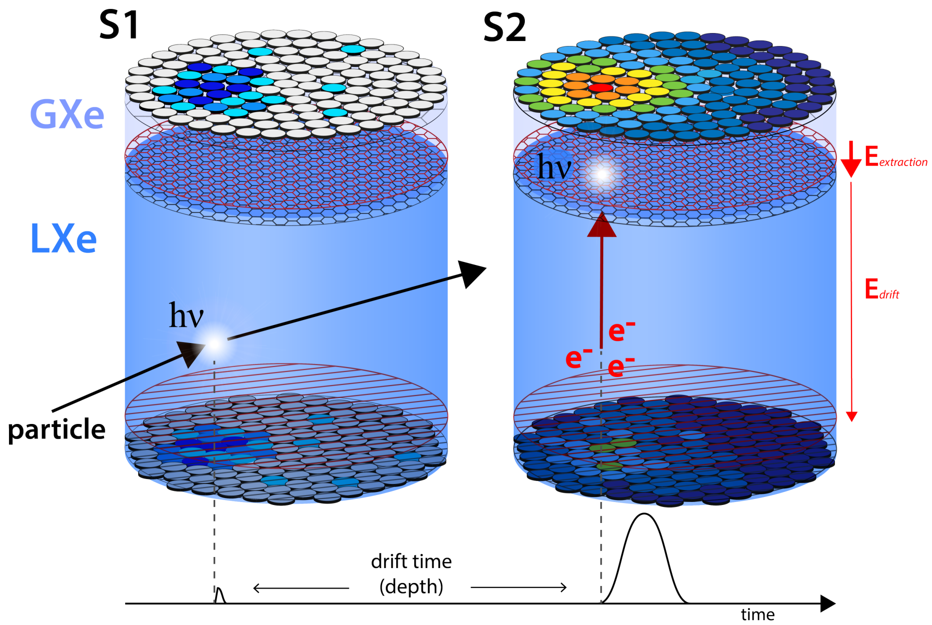

Figure 2.3: Signal generation and mode of operation of the cylindrical XENON1T dual phase TPC. Signal 1 (S1) is generated by the prompt scintillation light of the liquid xenon (LXe) and is detected by both photomultiplier arrays at the top and bottom. Signal S2 is based on ionization charges drifting because of the applied voltage to the top and are extracted at the liquid gaseous interface to the gaseous xenon (GXe). A strong extraction field accelerates the electrons which thus create another scintillation light proportional to the number of charges. Spatial reconstruction of the event is possible because of the S2 as the horizontal coordinates and the drift time between S1 and S2 being proportional to the interaction depth. [32]

An example for a dual phase TPC filled with xenon is shown in Figure 2.3 [32]. The cylindrical volume is almost completely filled with liquid xenon (LXe) and has at the top a layer of gaseous xenon (GXe). Xenon is commonly used because of its high atomic mass and thus preventing a high cross section for completely absorption of interacting particles and shielding against extrinsic ionizing radiation. The walls are designed for high reflectivity of the scintillation light. At the top and at the bottom of the volume are photomultiplier tubes for detecting the signals. These signals are created as follows: An incoming particle hits the xenon and due to recombination of the excited atom a prompt scintillation light at 178 nm arises which is called signal 1 (S1). Additionally, ionization electrons are generated by the collision which drift to the top of the detector because of the applied voltage by many wires in the volume. The drift electrons are accelerated to the liquid gas interface and get extracted by a stronger electric field. Now they produce a second scintillation light (S2) in the GXe, which has another shape than the S1 and is proportional to the number of electrons. From the S2 one can gather the position orthogonal to the drift field, called x and y in orthonormal coordinates. The z coordinate is calculated from the time difference between S1 and S2. This spatial resolution enables reducing the background for example by rejecting disturbing events from the detector walls where the drift field is too inhomogeneous. [12, 33]

The incoming particle can also interact multiple times with the xenon and in this way produce many S1s and S2s. Although these multi scatter events produce also only one S1 in the detector, because the prompt S1 is too fast and often diffuse because of reflections at the wall, the S2s have the possibility to be distinguished. Another event discrimination is possible regarding the type of interaction with the scintillator. The particle can mainly interact with the nucleus and produce a *nuclear recoil* or it can deposit its energy mainly in the electrons and produce an *electronic recoil*. The ratio between S1 and S2 is different so an ER deposits more energy in the ionization charges responsible for S2. This differentiation is important because the theory of dark matter predicts for a WIMP a NR and most background signals based on ERs can be excluded. [12, 33, 34]

2.3 Direct detection with XENONnT

The XENONnT dark matter experiment [20] uses a dual phase 8.5 t xenon TPC for direct detection of WIMPs. It is located at the INFN Laboratori Nazionali del Gran Sasso (LNGS) 1400 m (3600 m water equivalent) underneath the ground level for preventing disturbances by cosmic rays. Its main experimental components especially for keeping a low signal background will be described in the following. More detailed descriptions are available for the TPC [20, 23], the muon veto [35], the neutron veto [20] and the xenon handling system [23, 26, 36] in the references.

In Figure 2.4 at the left the XENONnT TPC is shown. The cylindrical volume has a height of 1.49 m and a diameter of 1.33 m. It is filled with LXe at a temperature of $-96\,°\mathrm{C}$ and a pressure of 1.9 bar which corresponds to a density of $2861.9\,\frac{\mathrm{kg}}{\mathrm{m}^3}$ [37]. At the top are 253 hexagonal PMTs, at the bottom 241 and the wall is made of high reflective polytetrafluoroethylene (PTFE).

For a better background reduction the cryostat and the TPC are surrounded by water and PMTs in a first layer by a neutron veto and in a second layer by a muon veto, which is shown in 2.4 [18] at the right. The neutron veto is going to be filled with high neutron capture cross section Gadolinium doped water in the future for registering external neutron radiation. But in this work only pure water was used. The neutron veto is enclosed in the muon veto which is a water Cherenkov detector registering external muons.

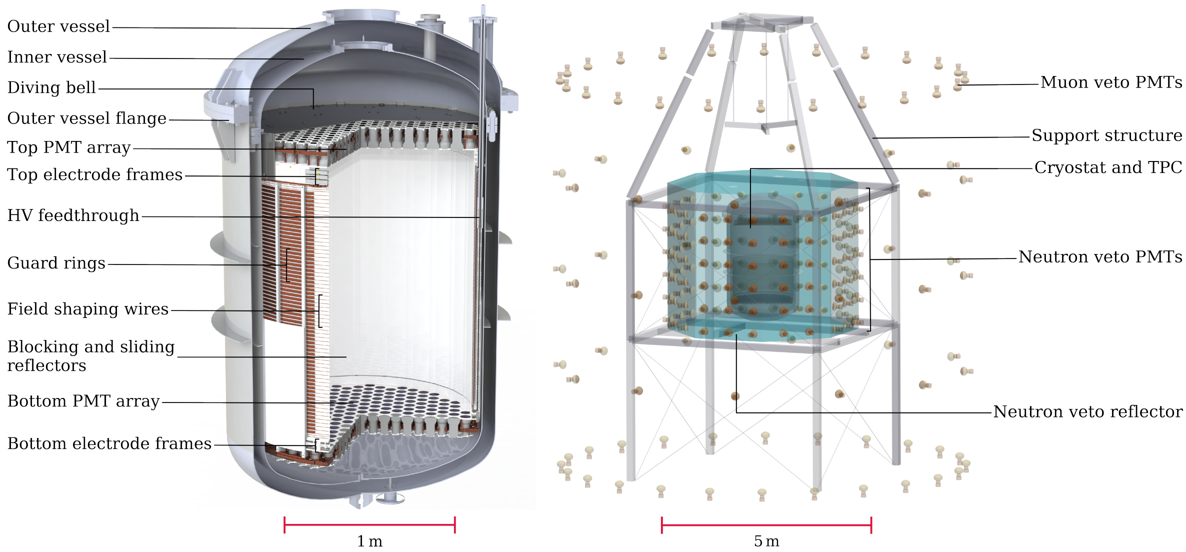

Figure 2.4: Schema of the three contributing detectors for XENONnT. Left the construction of the TPC with a height of 1.49 m and a diameter of 1.33 m. Left the embedding of the TPC in the neutron veto, an octagonal enclosure filled with water with an apothem of 2 m and a height of 3 m. This veto is centered in the Cherenkov muon veto which is a cylinder with 9.6 m in diameter 10.2 m high. The vetos are surrounded by PMTs for detecting the respective background sources. [18]

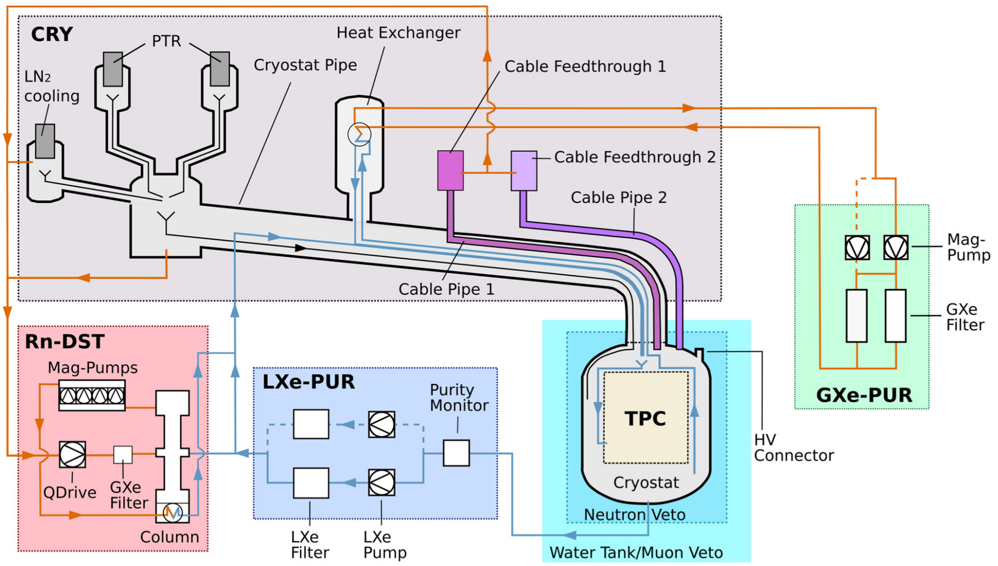

Figure 2.5: Schema of the xenon handling system for XENONnT consisting of the TPC and the cryostat, the cryogenics (CRY), the liquid (LXe-PUR) and gaseous (GXe-PUR) purification system and the online radon distillation (Rn-DST). The purification systems remove electronegative impurities from the respective phase of the TPC by using filters. The CRY controls the thermodynamic values of the xenon. The Rn-DST distillates radon with lower vapor pressure than xenon out of the circulating xenon. [23]

For minimizing the internal backgrounds coming from radioactive isotopes and removing electronegative impurities, the purification system and the radon distillation are coupled to the cryostat. The whole xenon handling system is shown in Figure 2.5 [23] where one can see the liquid and gaseous purification system (LXe-PUR and GXe-PUR) which remove constantly electronegative impurities by using filters. The cryogenic system (CRY) is used for liquefying, controlling and refilling xenon. The newly introduced online radon distillation (Rn-DST) [26] uses the lower vapor pressure of radon comparing xenon to remove this radioactive perturbation. A more detailed description of the system will be given in section 3.2. [23, 36]

3 Backgrounds and reduction methods

As presented before, the XENONnT experiment has better chances to detect the rare WIMP events the lower the background level. The external backgrounds like neutrons, neutrinos and muons have already been reduces by the underground location, the muon veto and the neutron veto. Additionally, the self-shielding mechanism of the xenon leads to the typical interaction point of the external background near the wall, which can be identified because of the spatial resolution. But on the other hand, intrinsic backgrounds from natural abundances of radioactive isotopes affect the sensitivity more. The different types and the previous reduction operations will be shown first. Especially, the new developed online radon removal will be presented. After that, it will be introduced how the background level can be determined. [18]

3.1 Intrinsic backgrounds and their reduction

Most intrinsic backgrounds interact via an electronic recoil, whereas the WIMP signal should be a nuclear recoil and thus should be distinguishable by using a TPC, but so called *accidential coincidences* (ACs), events falsely reconstructed by matching S1 and S2 from different sources, should also be minimized. The WIMP region of interest (ROI) for the ER interactions is from 1 keV to 13 keV. The ER backgrounds arise mostly from natural abundances of radioactive isotopes in the experimental material. We will group them in the category of the solid radiating materials and others which are liquid or gaseous. [18]

First, most of the intrinsic backgrounds by solid materials radiating in the detector can be found in the detector wall and the PMTs namely ^{238}U, ^{235}U, ^{228}Ra, ^{226}Ra, ^{228}Th, ^{137}Cs, ^{40}K and ^{60}Co and isotopes of their decay chains. α, β and γ radiation is mainly self-shielded by the xenon so the events occur only at the outer TPC or in the GXe. Therefore, one can use the *fiducialization*, so using only the inner volume, to reject those backgrounds in the analysis. On the other hand, these isotopes can produce neutrons by spontaneous fission or (α/n) reactions which are not affected by the self-shielding. But these events can be monitored in the future by the neutron veto. Although all of these events can be identified not to be a WIMP, ACs lead to a lower performance. Therefore, the *radioassay program* has been developed to minimize the particular isotope concentrations by monitoring the radioactivity of every part of the detector and choose only components with low activity. The individual values can be seen at [38]. [23]

The other intrinsic background source consists of gaseous and radioactive isotopes like ^{136}Xe, ^{124}Xe, ^{222}Rn, ^{85}Kr and ^{222}Rn. As they are not solid, they overcome the self-shielding and can diffuse through the whole handling system. Therefore, the sources have to be eliminated as good as possible.

^{136}Xe has a natural abundance of 8.9 % and decays by a double β^- emission, hence it has a relatively high half-life of $2.17 \cdot 10^{21}$ y. It contributes to the background in the ROI from 1 keV to 13 keV with an average rate of 1.3 (keV t y)$^{-1}$. The other relevant xenon isotope is ^{124}Xe whose double electron capture has been first observed by the XENON experiment. Its half-life of $1.4 \cdot 10^{22}$ y results also in a relative low activity of 3.7 (t y)$^{-1}$ at mainly two known peaks. Removing the xenon isotopes is relative complex and because of the small contribution to the low energy background their presence is accepted. [18, 21]

Krypton is contained in commercially available xenon with a concentration of 1 ppm to 10 ppb. A part of typically $\mathcal{O}(10^{-11})$ is the β^- emitter ^{85}Kr which was one main contributing background for the WIMP search. For reducing this, a cryogenic distillation column was established with which the whole xenon was distilled before filling the experiment. The concentration of krypton was reduced to (56 ± 36) ppq which is around 6 orders of magnitude lower than in the delivered xenon. The corresponding abundance of ^{85}Kr/$^{\text{nat}}$Kr in XENONnT was measured to be $\approx 2 \cdot 10^{-11}$ which results in a background of 1.1 (keV t y)$^{-1}$. [18, 20, 23, 36]

The leading background in the low ER from 1 keV to 30 keV, including the WIMP ROI, is introduced by ^{222}Rn. Other radon isotopes have a smaller abundance (<1 %) and can thus be neglected, whereas ^{222}Rn is constantly emanated by ^{226}Ra out of the detector components. The decay chain is shown in Figure 3.1 [25]. Due to its half-life of 3.8 d, it is homogeneously distributed in the whole xenon, independent from which component in the handling system it originates. ^{222}Rn itself is an α emitter at 5.6 MeV but the daughter ^{214}Pb with a short half-life of 26.8 min is responsible for a nearly constant low ER background by β^- radiation. It is generated in the decay chain after an α decay of ^{218}Po at 6.1 MeV also with a short half-life of 3.1 min. After the ^{214}Pb decays, a quick β^- decay by ^{214}Bi with half-life of 19.9 min and a very quick α decay by ^{214}Po with half-life of 164 μs at 7.8 MeV happen until the long living

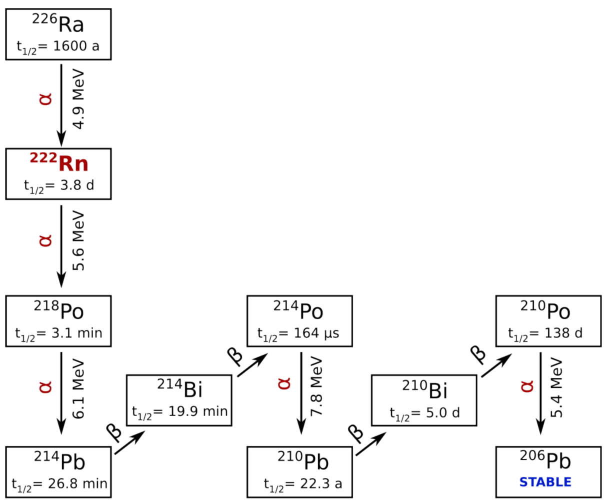

Figure 3.1: Part of the $4n + 2$ decay chain consisting ^{222}Rn generated by ^{226}Ra. [25]

^{210}Pb with half-life of 22.3 y is generated. The short half-life of ^{214}Po leads to special signature of the *BiPo* events so that the previous β decay of ^{214}Bi can be removed in analysis. The ^{214}Pb features no such coincidence so the amount of radon emanating materials has to be reduced. Measuring the emanation rates [25, 39, 40] and selecting for the best materials became a central task. The current emanation rate gives a ^{222}Rn activity of 4.2 $\left(^{+0.5}_{-0.7}\right)$ μBq/kg [23], but XENONnT has a goal of $< 1\,\mu$Bq/kg so the permanently emanated radon has to be removed online resulting in an equilibrium. The removing is performed by a cryogenic distillation system which will be presented in the next section. It reduced the activity in a first step to 1.7 μBq/kg [18, 20, 22, 23, 26, 41]

As a summary, the intrinsic backgrounds not affected by the self-shielding do the largest contribution to the ER background until 140 keV. The latest ER background fit from the first science run (SR0) of XENONnT is shown in Figure 3.2 [20]. Belonging to the background model are ^{214}Pb, ^{136}Xe, ^{133}Xe, ^{124}Xe and ^{85}Kr. The on purpose introduced calibration source $^{83\mathrm{m}}$Kr shows only one peak at ≈ 38 keV. The background from the materials has in the fiducial volume only a small constant contribution of $2\,(\mathrm{t\,y\,keV})^{-1}$. And the only small external background by solar neutrinos is also around $2\,(\mathrm{t\,y\,keV})^{-1}$ and can not be avoided easily. ^{85}Kr is strongly suppressed and only contributes with a constant background of $< 1\,(\mathrm{t\,y\,keV})^{-1}$. Dominating backgrounds beyond the ROI (1,13) keV are ^{136}Xe, ^{133}Xe and ^{124}Xe. But still dominating source in the ROI is ^{214}Pb with a contribution of $5\,(\mathrm{t\,y\,keV})^{-1}$, although the result shown here has a ^{222}Rn activity of 1.7 μBq/kg. Therefore, it is crucial to further reduce the ^{222}Rn activity.

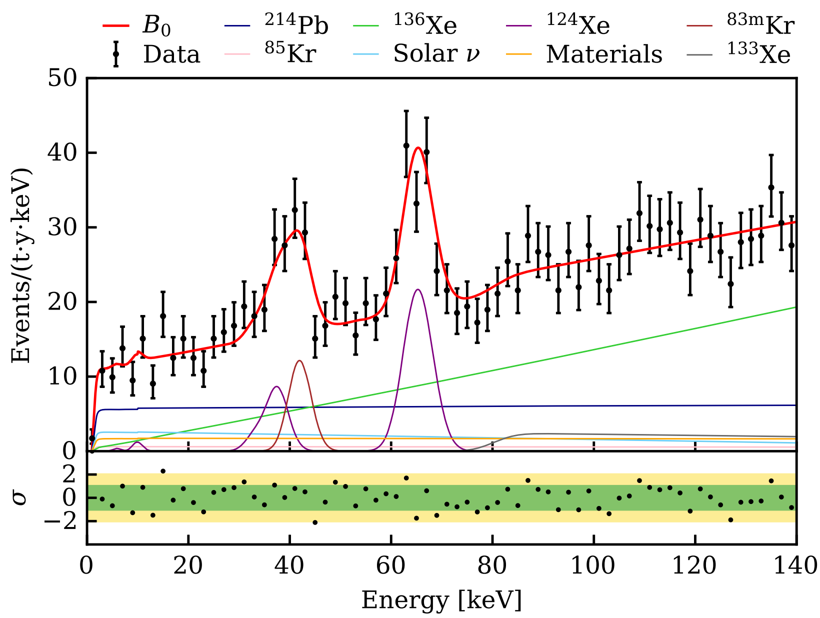

Figure 3.2: Fitted ER background model B_0 of XENONnT SR0. The dominating background in the ROI (1,13) keV is ^{214}Pb with a constant contribution of $5\,(\mathrm{t\,y\,keV})^{-1}$ at a ^{222}Rn activity of 1.7 μBq/kg. [20]

3.2 Radon background reduction by online distillation

As it became clear in the previous section, reducing the ^{222}Rn activity is one main goal for reaching the best sensitivity. If the emanation is reduced at its best by selecting low emanating materials, one has to constantly remove the radon. It is done by a cryogenic online distillation [26] which was first demonstrated in one previous experiment XENON100 [24]. The concept and the currently used radon removal system will be shortly introduced in the following.

The radon removal system (RSS) is based on a McCabe-Thiele approach which traps the liquefied radon at the bottom of a tower and extracts gaseous xenon at the top. The trapped radon decays with its half-life of 3.8 d so this concept works without any extraction and thus any loss of xenon. The schematic method of a distillation tower with a reboiler at the bottom and a condenser at the top is shown in Figure 3.3. Liquid streams are dark blue, gaseous streams light blue and the radon symbolized by the green dots. The tower is divided into three parts: the lower stripping section with the reboiler, the middle feeding section with the inlet and the upper rectifying section with the condenser and the outlet. The inlet in the middle left of the tower with stream F can insert contaminated LXe with stream qF and GXe with stream $(1-q)\,F$. The LXe streams downwards to the reboiler and the GXe upwards to the condenser. The streams of the LXe or GXe are in the stripping or rectifying section L'/L respectively V'/V.

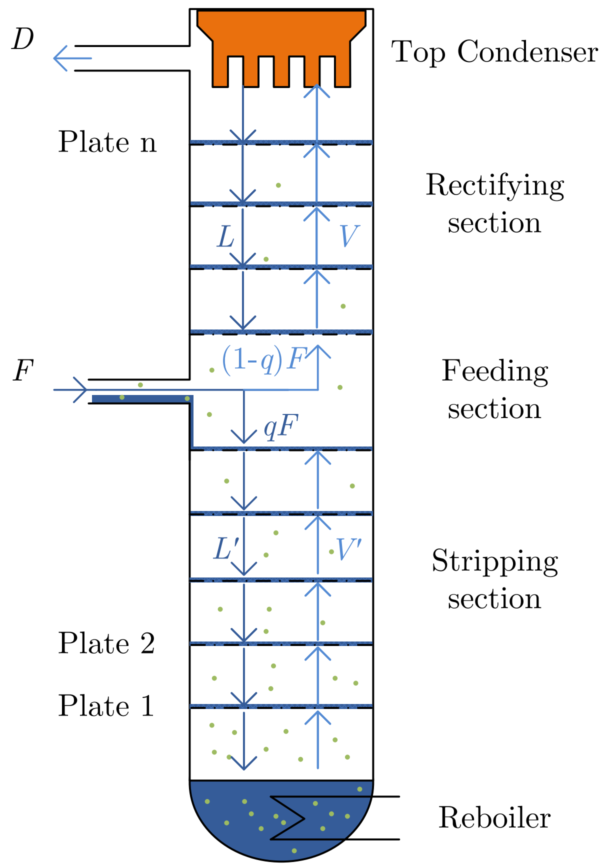

Figure 3.3: Concept of a McCabe-Thiele distillation method without extraction of the contaminant. Liquid (gaseous) streams are dark (light) blue, green dots represent the contaminant. At the top of the distillation column is a condenser and at the bottom a reboiler. Between stay n plates for the distillation stages. The contaminant is enriched in the bottom stripping section, the feeding section is the inlet of the contaminated liquid/gas and at the top rectifying section the contaminant is depleted where a fraction of purified gas streams out. [26]

An arbitrary number of plates n acts as distillation stages. These ensure a heat exchange between up- and downstream, which leads to a liquefaction of upstreaming gaseous radon and boiling of downstreaming LXe. In a single stage a radon reduction of $\frac{1}{\alpha} = \frac{P_{\mathrm{Xe}}}{P_{\mathrm{Rn}}} = 10$ at $-98\,°\mathrm{C}$ is performed, which is based on the ratio of the vapor pressures P of the two contributing gases. The purified xenon at the top can be either stream out with stream D or be condensed and injected to the recirculation with stream L. For reducing the activity from the initial $4.25\,\mu\mathrm{Bq/kg}$ to $< 1\,\mu\mathrm{Bq/kg}$, a destination flow of $F = D = 71\,\mathrm{kg/h}$ (200 slpm (standard liter per minute)) was set. [26]

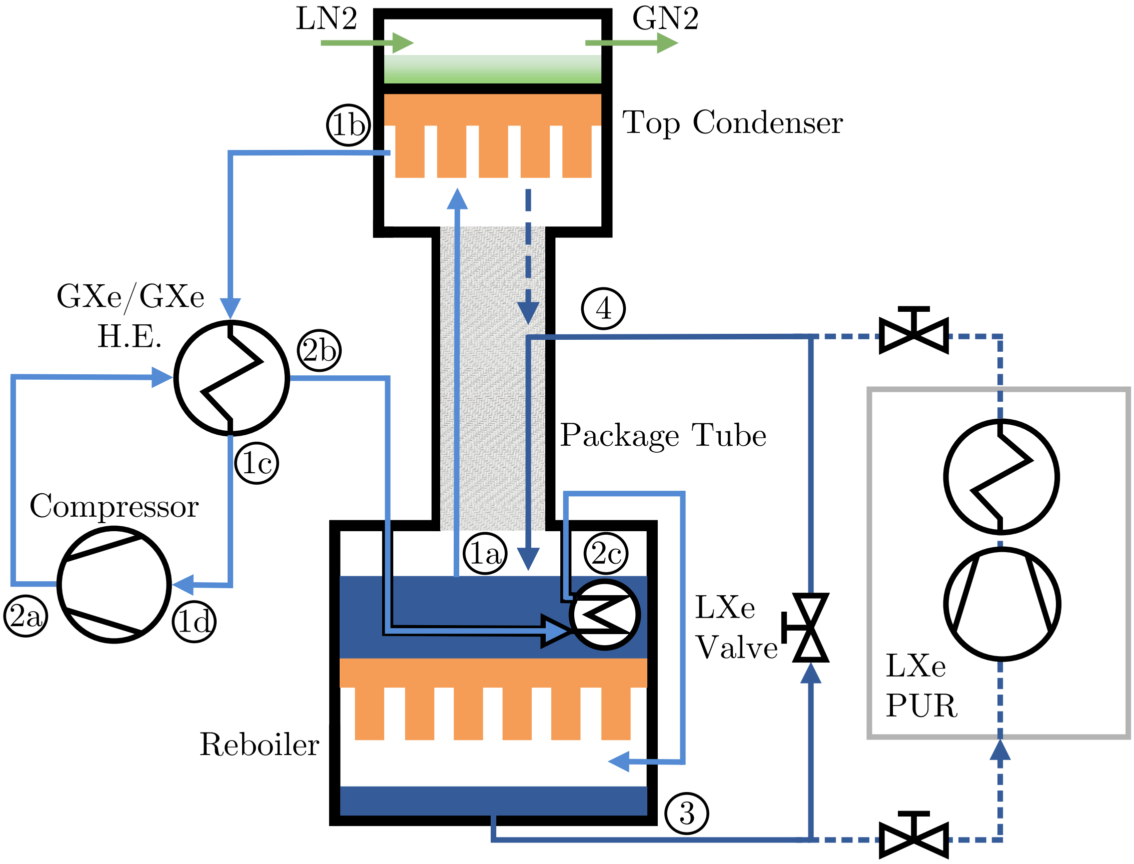

Figure 3.4: LXe (dark blue) and GXe (light blue) flows within the radon removal system. The Claudius-Rankine cycle (heating, compression, cooling, expansion) of the circulating xenon supports the coupling of the needed cooling and heating power. [26]

Based on the theoretical concept, the RRS was constructed to extract a fraction of LXe from the purification system on the one hand and on the other hand GXe from the gaseous phase in the TPC which was liquefied before by the CRY (see Figure 2.5). The two operation modes should both reduce the activity by a factor of ≈ 2. The implemented RRS with its gas (light blue) and liquid (dark blue) flows is shown in Figure 3.4 [26]. The theoretical plates in the distillation column from Figure 3.3 were changed to a package material with large surface for high energy exchange similar did in [36] with the same material [42]. The xenon flows through a thermodynamic Claudius-Rankine cycle (number 1 to 4) to couple the needed heat and cooling power (each 3 kW) so that the needed liquid nitrogen (LN2) for cooling and the electrical power in the reboiler is minimized. The cycle in the LXe mode works as follows: **1a** LXe gets boiled and thus streams upwards through the packing material of the distillation column. A part of it is condenses at the copper fins cooled by LN2 and recirculates, the other part **1b** streams out to a heat exchanger (HE) **1c** where it is heated by other GXe to room temperature for getting compressed **1d**. The compressed and warmed-up GXe **2a** streams back to the HE and is cooled down in a first sequence **2b** by the incoming GXe from step **1c**. It is cooled down in a second stage in a spiral HE **2c** which is located in the liquid phase of the column at the top reboiler. After that, the still gaseous and compressed xenon streams further to the volume at the bottom reboiler where it condenses at the copper fins **3** which guarantee an energy exchange to the LXe in the top reboiler. At the end of the cycle, liquefied xenon streams either through a bypass again in the distillation column and expanses **4** or is returned to the LXe PUR. The bypass was only applied for testing the RRS without the other components of the experiment. For best performance at a flow of 71 kg/h (200 slpm), a powerful and low emanating compressor has to be used. Therefore, a four-cylinder magnetically-coupled piston pump (4MP) [43] was constructed. [26]

All in all, the RRS reached a flow of (91 ± 2) kg/h ((258 ± 6) slpm) which should result in a reduction factor of 4.7 for reaching the goal activity of $< 1\,\mu$Bq/kg. During SR0 of XENONnT, only the GXe mode could be applied because the LXe induced too much electronegative impurities. A reduction down to $1.7\,\mu$Bq/kg was accomplished in this way. After SR0, the LXe mode could be additionally introduced which resulted in the destined $< 1\,\mu$Bq/kg. [20, 26]

3.3 Background monitoring

For checking whether the RRS or switching materials have led to a lower ^{222}Rn activity, one has to monitor it, like it will be presented in chapter 4. The general concept of this analysis and how to do it is described in the following.

Finally, we want to estimate the background induced by ^{214}Pb. A direct energy solved detection of the continuous β spectrum is complex and disturbed by other decays (see Figure 3.2) but the α decay rate of ^{218}Po at 6.1 MeV and ^{214}Po at 7.8 MeV give a good upper and lower limit, because the decay chain runs relatively quick. Due to the high energies and the mono energetic α decay and hence such a S1, less disturbances interfere their screening. ^{214}Po, which gives the lower limit, has a very short half-life of $164\,\mu$s and therefore can be merged with the previous ^{214}Bi, as already presented in section 3.1.

But the ^{214}Bi decay usually generates multiple S2s which lead to a wrong S1/S2 merging of the ^{214}Po and so to a wrong drift time and positional reconstruction. Therefore, the signals have to be individually merged, which represents an own analysis not done here. Another method would be an S1 only analysis like in [44] which would require more own corrections and removing of e.g. wall background events which are usually identified by positional reconstruction.

Only the estimation of the upper limit by ^{218}Po with usage of S2 will be done. For this, first the signals of the PMTs have to be processed to built up events and their variables. For this purpose, the data processor STRAXEN (streaming analysis for XENONnT) [45] calculates th high level data including events with matched S1s/S2s. In a next step, the data can be corrected for e.g. dependencies of the S1 on geometric effects, done every two weeks by the well-known coincident decay lines of $^{83\mathrm{m}}$Kr at 32.2 keV and 9.4 keV [46], which should result in a fixed value for S1 at any place in the detector. Other corrections are done concerning the field inhomogeneity, electron extraction out of the LXe and further electrical effects. After these corrections, S1/S2 turn to cS1/cS2. [20]

Before the events are analyzed, usually *basic quality cuts* are applied for removing noise and falsely merged events or to set a ROI. After that, sometimes further own corrections have to be done because the corrections done by STRAXEN are optimized for the low energy range. At the end, the Gaussian peak area of the cS1 α spectrum can be fitted as a value for the events. The whole procedure will be presented in the next chapter.

4 Radon background estimation

The published ^{222}Rn activity of $1.7\,\mu$Bq/kg[1] during the first science run SR0 will be checked by taking a different approach than the original analysis. The published value was estimated by using both a S1-only approach and a S1 and S2 analysis. Both used an own S1 correction and a “by eye” data selection. After that, the peaks were fitted with an unbinned likelihood method. In this analysis, a S1 and S2 analysis will be done by using the corrections from STRAXEN 1.7.2. Only a few data cuts which only lower the background and not affect the signal will be applied in section 4.1. Small additional corrections will be added in section 4.2 to shape peaks more Gaussian-like and at least the spectrum will be fitted in section 4.3 with a Poisson-likelihood chi-square function [47] using the minimization tool iminuit [48]. Based on that, the reduction of the ^{222}Rn activity will be calculated in subsection 4.3.4.

Although the α analysis is done in the high energy regime and therefore has less disturbing signals, some background arising from ^{220}Rn at 6,4 keV and its daughter ^{212}Bi at 6,2 keV affects the signal of ^{218}Po at 6,1 keV. Moreover, ^{220}Rn was introduced as a high activity calibration source during SR0 and thus its usual $> 100\times$ lower rate [18] was increased before taking science data. Additionally, the usage of less cuts leads to more background which should be considered in the background model. As a consequence, the spectrum parameters of peak width and position have to be well known for limiting them in the fits with *constraints*. These are additional parabolic terms to the cost function of a custom amplitude which can act as a local minimum. The values for the constraints of ^{220}Rn and ^{212}Bi will be determined by using also the ^{220}Rn calibration data in section 4.3.

4.1 Applied data cuts for extraction of usable data

Cutting data for an analysis is crucial in order to remove background or to have more computing resources by loading less data. In Figure 4.1 the whole data spectrum taken from XENONnT is shown in a cS1/cS2 two dimensional histogram in th units of PE (photoelectrons) with the number of entries for each bin. For this example, only background data was used so no large activity of calibration sources should be present. A band without any data at cS1 = 27 kPE is blinded for the neutrinoless double beta decay. Most of the data

[1]The original analysis gives this value for the ^{218}Po activity but this upper limit is always presented as the ^{222}Rn activity.

has cS1 < 30 kPE but the α decays are in the high energy ROI of 40 kPE < cS1 < 70 kPE, what is only 1.4 % of the whole data shown here. ^{222}Rn is located at 54 kPE and ^{218}Po at 59 kPE and both have a likely cS2 $= 2 \cdot 10^4$ PE. At smaller or higher cS2 are backgrounds from β or γ radiation of different isotopes.

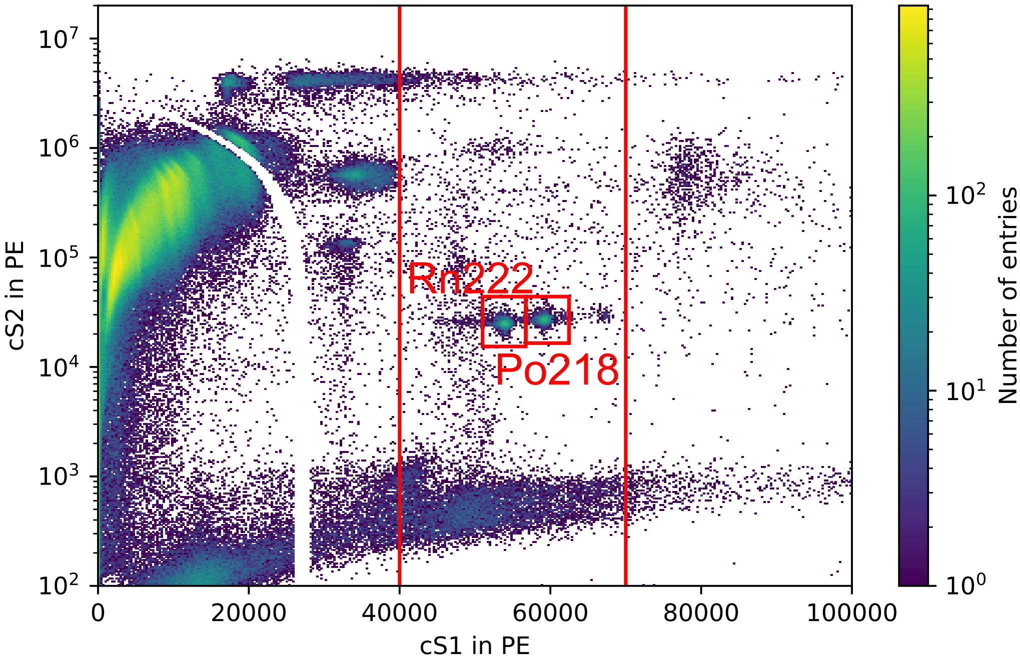

Figure 4.1: cS1/cS2 histogram of the whole spectrum in the unity of photoelectrons (PE). The band without data at cS1 = 27 kPE is blinded for the neutrinoless double beta decay. α decays are in the high energy ROI at 40 kPE < cS1 < 70 kPE, where ^{222}Rn is located at 54 kPE and ^{218}Po at 59 kPE with both cS2 $= 2 \cdot 10^4$ PE.

Drift time cut

A further reduction of unnecessary data can be archived by excluding the events appeared in the GXe. TPCs are planned for events in the LXe whose charges drift to the GXe whereas one can get no important information from gas events. They have all a relative low drift time and thus a limit of $t_{\mathrm{dt}} > 5 \cdot 10^4$ ns is set. In Figure 4.2 on top, the cut is shown in the drift time/S1 area fraction top (AFT) histogram. The AFT is a low level data parameter calculated via the fraction of the S1 detected at the top PMT array, why it is an additional indicator in which height the event happened.

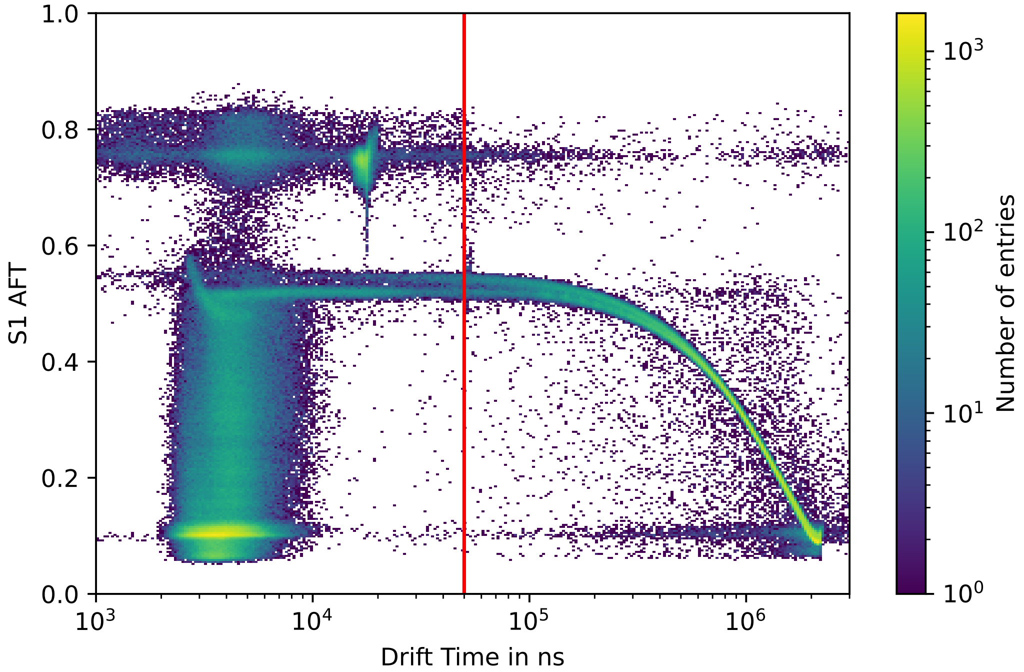

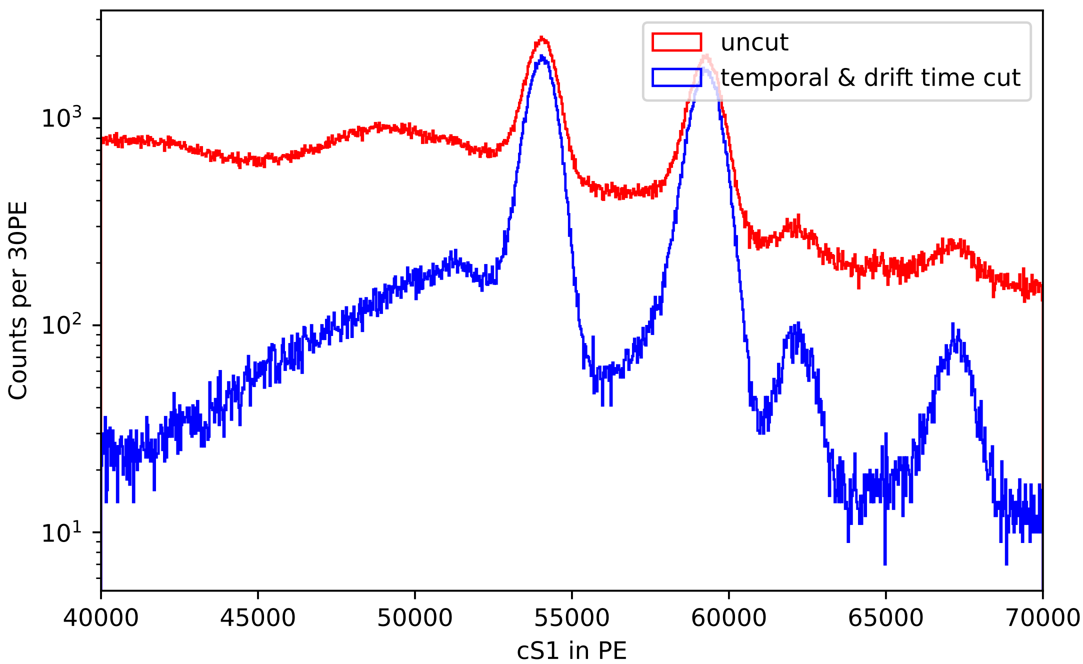

Figure 4.2: Applied drift time cut excluding gas events with $t_{\mathrm{dt}} < 5{\cdot}10^4$ ns. (Top) S1 area fraction top (AFT)/drift time histogram shows the excluded events. At the included events the correlation between S1 AFT and drift time is visible as a band. (Bottom) cS1 spectrum without and with the drift time cut. Applying the cut leads to removing of much background which leads to a better visibility of the α peaks of ^{222}Rn (54 kPE), ^{218}Po (59 kPE), ^{220}Rn (62 kPE) and ^{216}Po (67 kPE).

By applying this cut, 68 % of the events are excluded. The remaining events at higher drift times show the correlation of S1 AFT and drift time visible in a band. At the bottom of Figure 4.2 the cS1 spectra by using the cut are compared. The visibility of the ^{222}Rn and ^{218}Po peak is improved and another two peaks at 62 kPE and 67 kPE with a $> 20\times$ lower amplitude stay out which correspond to ^{220}Rn and ^{216}Po. But still a huge background at cS1 < 53 kPE dominates the spectrum.

S1 Area Fraction Top cut

As an additional cut for removing background, the S1 AFT cut, defined by the XENON collaboration [2] , will be applied on the ^{220}Rn data. The usage of it influences on the number of α peak events which does not matter regarding the ^{220}Rn data only used for getting constraints on peak width and position. The science data, for which the ^{222}Rn activity has to be calculated, would be too much influenced by this cut.

Like shown at the previous drift time cut, the S1 AFT and drift time have a correlation. The fraction of light which is collected by the top array P can be written as binomial distribution whether the whole light $S1$ detected with a probability AFT and a number $S1_{\mathrm{top}}$ at the top or with probability $(1 - AFT)$ at the bottom PMT array:

$$P = \frac{S1!}{S1_{\mathrm{top}}!(S1 - S1_{\mathrm{top}})!} \, AFT^{S1_{\mathrm{top}}} \, (1 - AFT)^{S1 - S1_{\mathrm{top}}} \tag{4.1}$$

where the factorial is translated to a Γ function because of the not integer like AFT to

$$P = \frac{\Gamma(S1 + 1)}{\Gamma(S1 - S1_{\mathrm{top}} + 1)\Gamma(S1_{\mathrm{top}} + 1)} AFT^{S1_{\mathrm{top}}}(1 - S1_{\mathrm{top}})^{S1 - S1_{\mathrm{top}}}. \tag{4.2}$$

The values for the probability AFT dependent on the drift time are extracted from geometrical effects which also occur in the S1 correction by using $^{83\mathrm{m}}$Kr. Another approach would be an optical simulation which has not been fully finished. To the resulting drift time dependence line an arbitrary deviation tolerance for included events is added where the value is set “by eye”.

[2] following definition available at internal communication and not published, only mentioned in [29, 49]

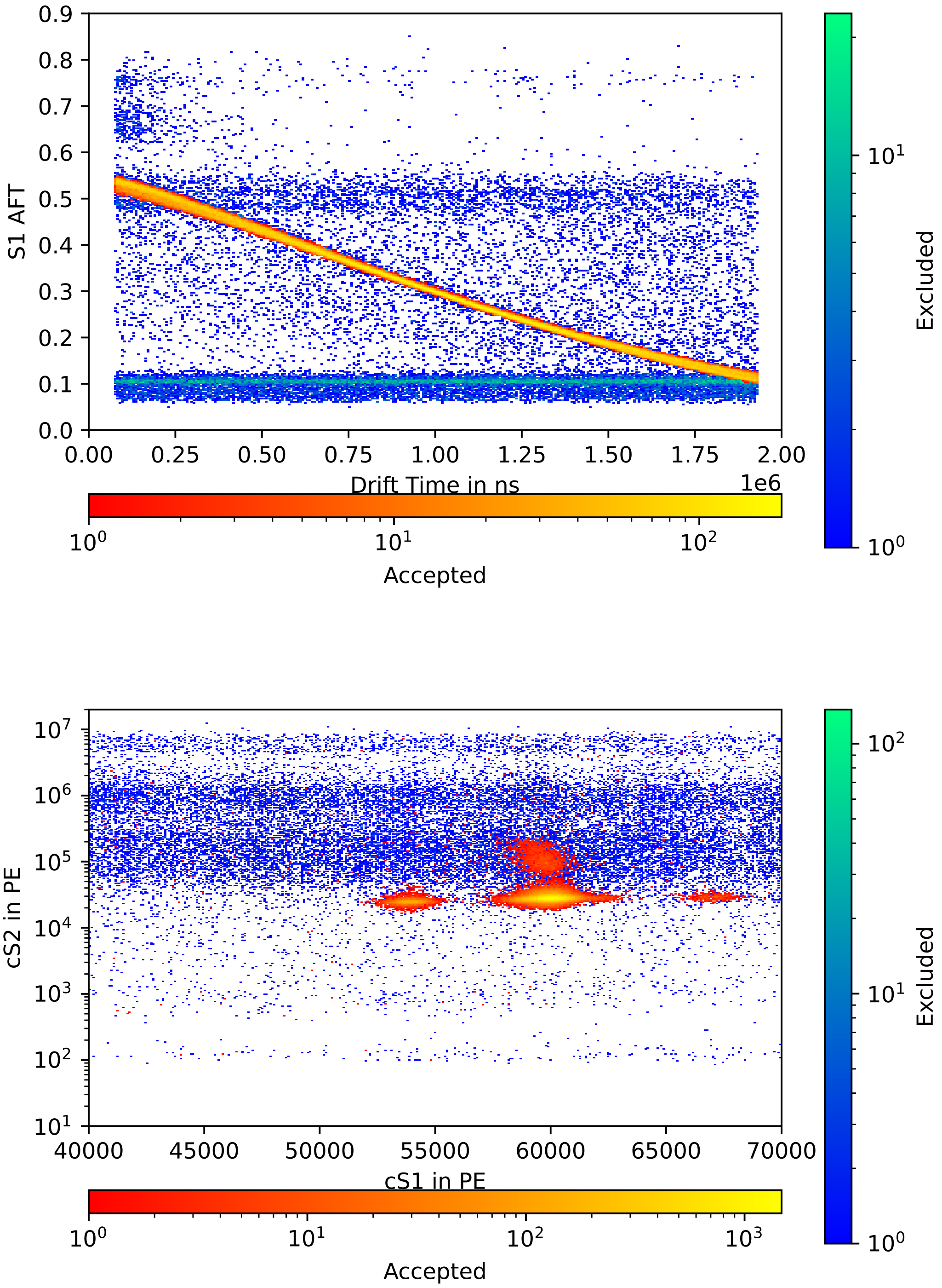

Figure 4.3: S1 area fraction top (AFT) cut applied on ^{220}Rn calibration data with accepted (red) and excluded (blue) events. (Top) S1 AFT/drift time histogram shows the accepted events within the linear dependence band. (Middle) In the cS1/cS2 parameter space, the background of the α peaks at $3 \cdot 10^4\,\mathrm{PE} < cS2 < 1 \cdot 10^7\,\mathrm{PE}$ is removed whereas the distinct populations are accepted. (Bottom) next page.

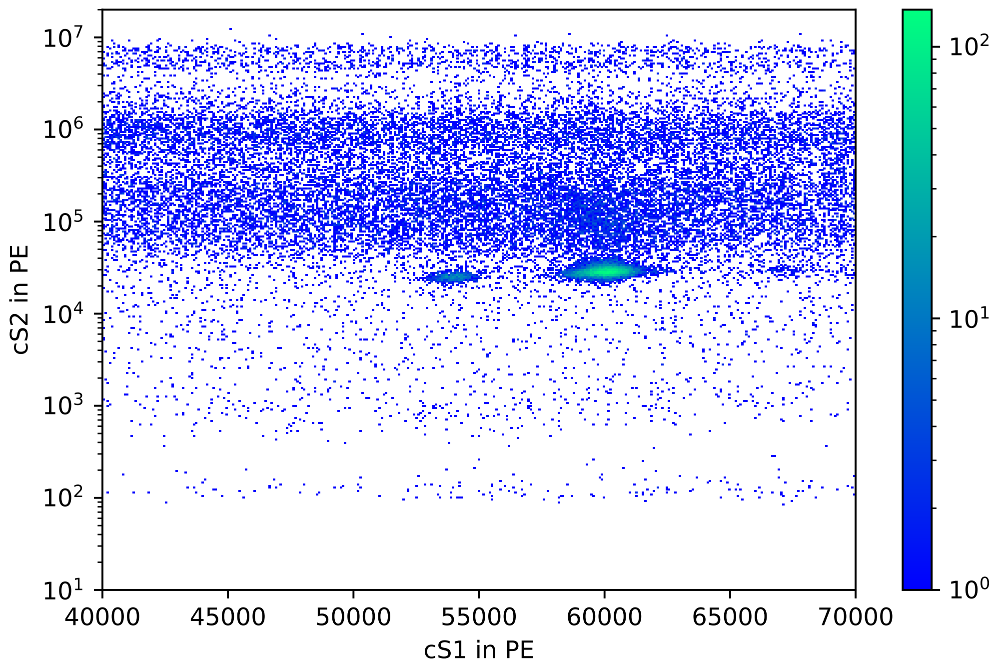

Figure 4.3: The cS1/cS2 histogram of the excluded events shows that the α populations are also partly removed by the S1 AFT cut.

The S1 AFT cut applied on ^{220}Rn data is shown in Figure 4.3 with the excluded data in blue and the accepted in red. In the top plot, the S1 AFT/ drift time histogram shows clearly the accepted band on data whereas the blue data shows an unphysical behavior and thus is excluded. This unphysical behavior can be based on ACs which appear especially at a high data rate like in a ^{220}Rn calibration. The middle plot shows the cs1/cs2 histogram from which a broad constant band of background in $3 \cdot 10^4\,\mathrm{PE} < cS2 < 1 \cdot 10^7\,\mathrm{PE}$ is removed. The background could originate from the involved β decays whose S1 is added by another α S1 and thus falsely reconstructed. However, the cut leaves the α peaks but as shown in bottom plot (next page), where only the excluded events are plotted, the cut also rejects events within the peak cs1/cs2 parameter space.

Loaded data

After reducing the amount of data to load, one can easily look at the whole SR0 data over time in the ROI shown as a cS1/time histogram in Figure 4.4. SR0 was from 1st May, 2021 to 30th November, 2021, where at the beginning only commissioning was executed and the science data began at 6th July, 2021. The head of the graphic shows at which time ^{220}Rn or ^{83m}Kr calibration data or background data was measured. ^{83m}Kr was used usually every 2 weeks for a calibration but ^{220}Rn only in the commissioning phase until end of June. Looking at the cS1 spectrum, one can see that the peak position of ^{222}Rn and ^{218}Po varies in the commissioning phase which is based on the *light yield* which describes how much S1 gets produced at which energy. During the science data the light yield stays constant. During the ^{220}Rn calibration a huge increase of activity can be seen at 60 kPE which corresponds to the activity of ^{212}Bi, a product of the decay chain. The activity drops after the calibration and during the science data only the background peaks of ^{220}Rn (62 kPE) and ^{216}Po (67 kPE) are visible. The other huge background which was not eliminated by the drift time cut is at cS1 $<$ 53 kPE. This corresponds to the wall background of ^{210}Po decaying with 5,4 keV and getting produced by the wall component ^{210}Pb. The background can thus be eliminated by using the xenon self-shielding and the spatial resolution of the TPC in a next step.

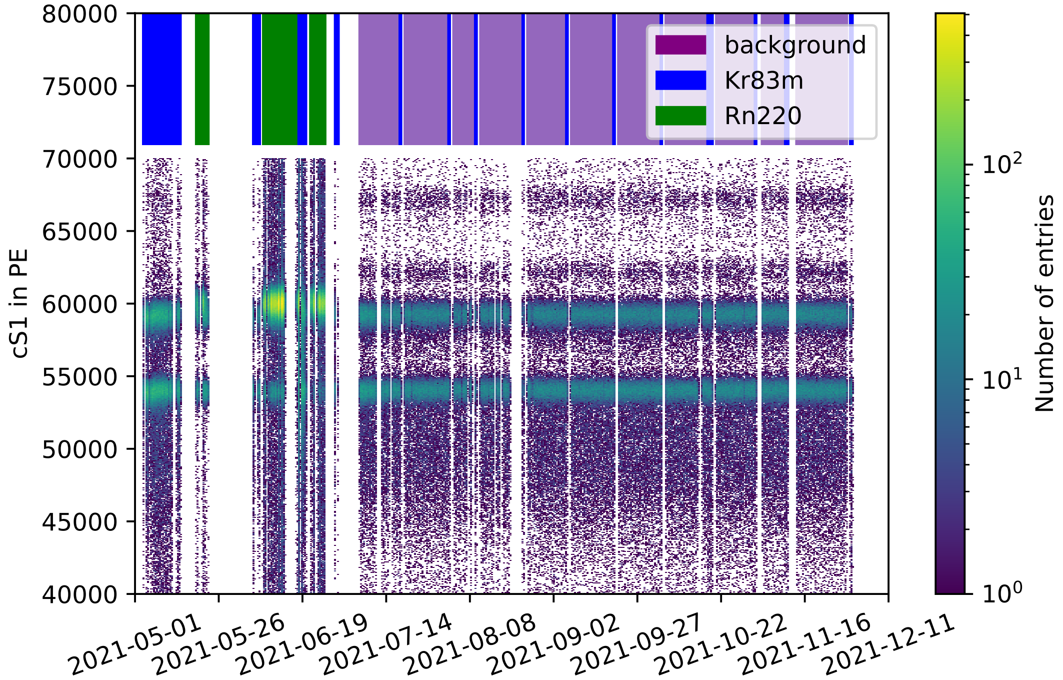

Figure 4.4: SR0 overview with belonging data taking modes of ^{83m}Kr and ^{220}Rn calibration data and background data. The α lines are homogeneously visible concerning the activity. During the commissioning phase before July an inconstant mean cS1 of the α lines is observable. Moreover, the ^{220}Rn introduces a high background until July. Furthermore, a constant background at cS1 $<$ 52 kPE is present over time.

Spatial cuts

As introduced before, a TPC features spatial resolution which can be used for fiducialization because field inhomogeneities and wall backgrounds can affect events occur in the outer parts. Moreover, only events occurred in the LXe and the electrical drift field can be used. This fiducialization is shown in Figure 4.5, where only events with -5 cm < Z < -130 cm and $R^2 < 4000\,\mathrm{cm}^2$ were accepted. For the following cuts the whole background and ^{83m}Kr data was used.

On top of Figure 4.5 the Z cut is shown where the α peaks are visible as slightly curved lines in the cut area. The events are homogeneously distributed along the peak line. Beyond the cut cS1 drops and therefore the events in these regions can not be used. At $Z > -80\,\mathrm{cm}$ the ^{210}Po background is visible at 50 kPE. Although ^{210}Po should be homogeneous distributed along the detector wall, it could be possible that it is only visible at higher Z because the corresponding S2 only reaches there the top PMT array. At lower Z the charges could drift into the wall because of the field inhomogeneity.

The R cut with data after applying the Z cut is shown on the bottom of Figure 4.5 as a cS1/ R^2 histogram. One can see directly the excluded events at mainly cS1 < 52 kPE which supports the origin of ^{210}Po as a wall background. The lines of the α peaks are once again visible with a homogeneous distribution of the events within the line. But all lines show an oscillating dependence of the cS1 on R^2, which could arise from the finite quality of the correction.

Summarizing the spatial cuts in Figure 4.6 the background was further reduced by removing ^{210}Po as a wall background. This can be seen in the top histogram especially in the top right corner and in the bottom cS1 spectrum at cS1 < 50 kPE after applying the R cut. A homogeneous distribution of the events in the fiducial volume was archived and now the α peaks have an amplitude of $> 200\times$ (^{222}Rn and ^{218}Po) and $> 10\times$ (^{220}Rn and ^{216}Po) higher than the background. But as already noted, the cS1 shows a dependence in Z and R which leads to a non-Gaussian peak shape and thus in a fewer compatible fit model and less robust fits when using Gaussian peaks. As a consequence, the dependencies have to be corrected before fitting the spectrum.

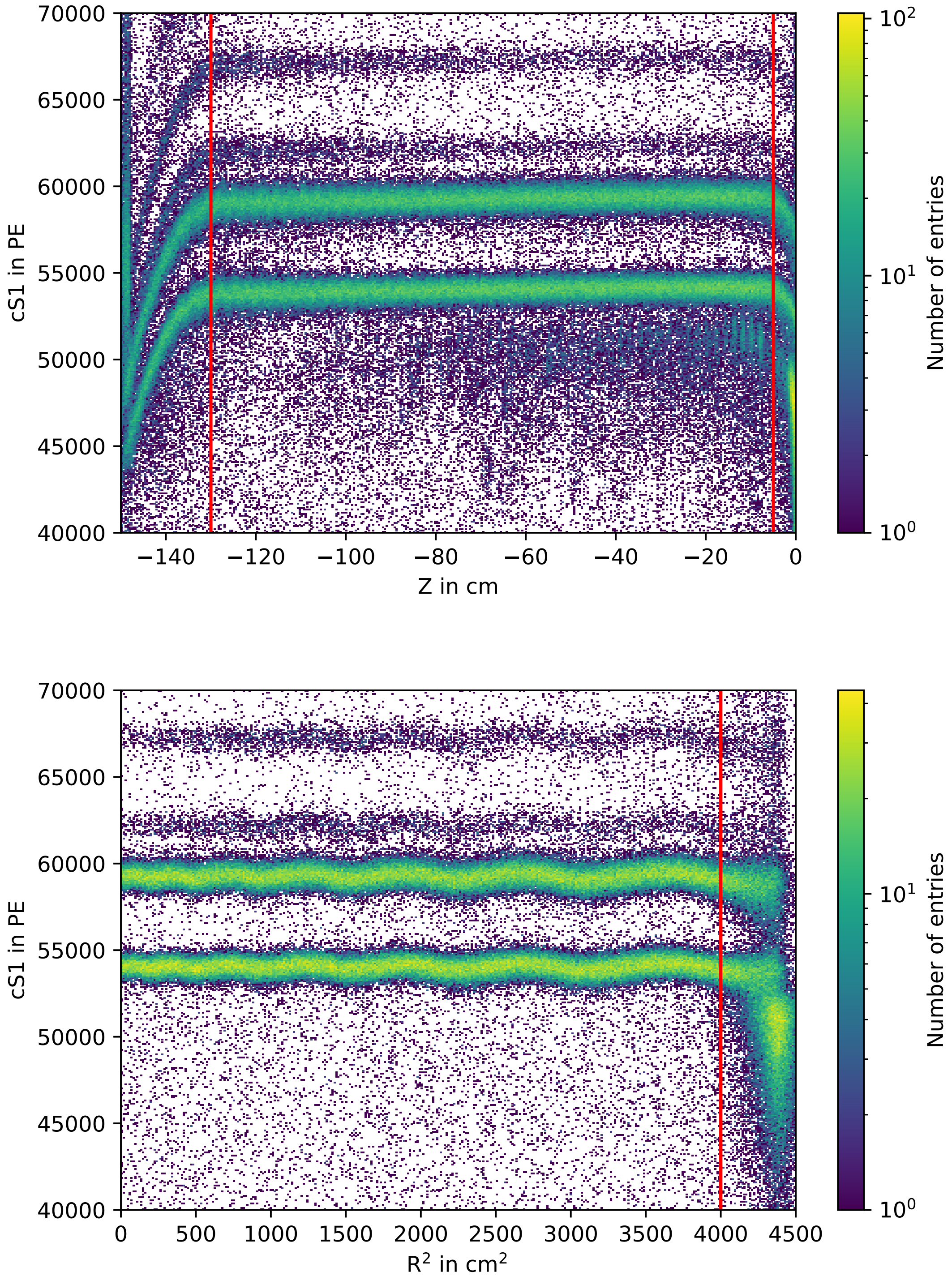

Figure 4.5: (Top) Z cut removes the on Z dependent cS1 events at Z < -130 cm and Z > -5 cm which arise from field inhomogeneities. (Bottom) R cut removes wall background at R > 4000 cm^2 below 52 kPE. The α lines show all the same oscillating R dependence.

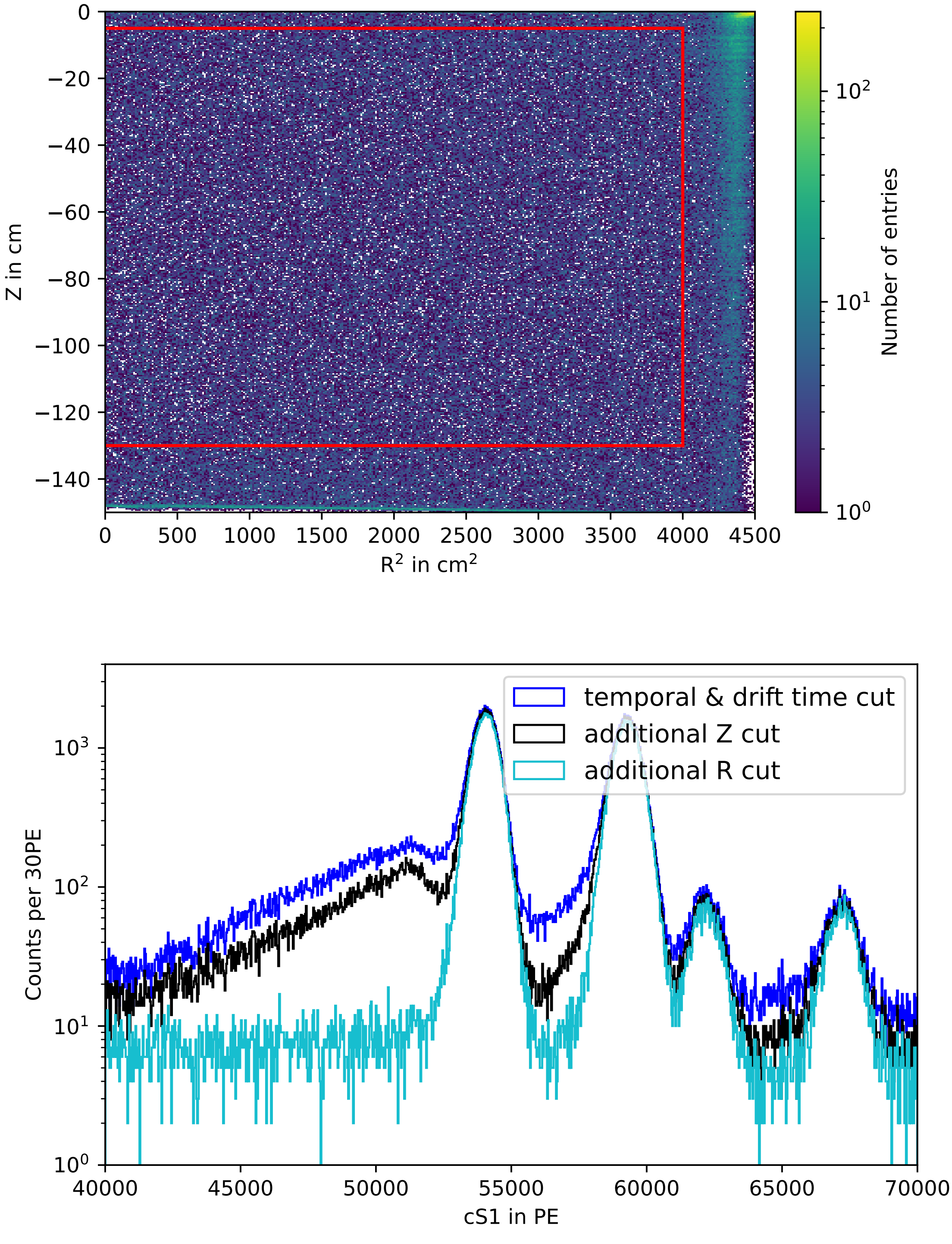

Figure 4.6: (Top) The fiducial volume of the analysis shows in a R/Z histogram a homogeneously distribution of the events. At low Z and high R the wall background by ^{216}Po can be observed. (Bottom) cS1 spectra before and after the spatial cuts. The Z cut removes background all around the peaks whereas the R cut especially removes the background at $< 52\,\mathrm{kPE}$ so that the α peaks reach a higher visibility.

4.2 cS1 peak shape corrections

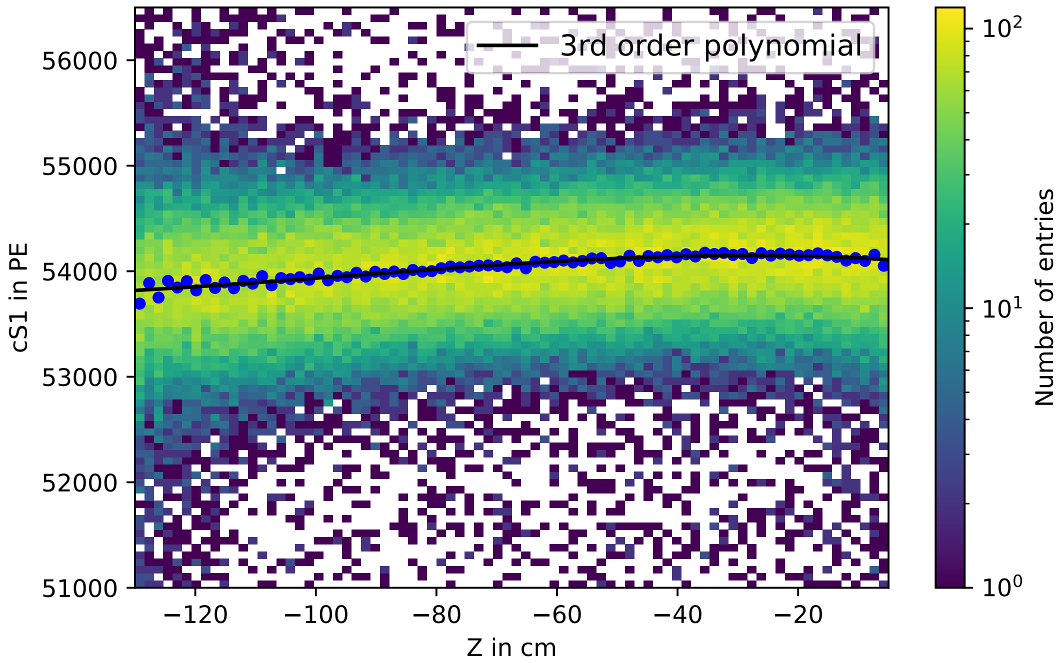

Figure 4.7: cS1/Z histogram shows the dependence and the fitted mean values of the Z slices with a 3$^{\text{rd}}$ order polynomial. The fit matches the data.

In the previous section it was demonstrated that the cS1 shows dependencies on Z and R which originate from the imperfect corrections. Using the current values for cS1 resulted in spectrum fitting difficulties because of the peak shape. For this reason an own additional correction on Z and R will be applied in the following turning cS1 to ccS1, which will improve the Gaussian-like peak shape. The procedure for a correction is to find a function describing the dependence, then fit it to the data and set all the data to the same arbitrary value using the function. In this work, the ^{222}Rn line was selected in the 2d histogram and for every Z or R bin the mean cS1 value was calculated. The errors of the fitted mean values are set inverse proportional to the counts of the bin and are fitted with a least square method. The fit parameters are given in the appendix.

Figure 4.7 shows the fitted Z dependence in a cS1/Z histogram. The histogram was divided in 80 Z slices whose mean cS1 were fitted with a 3$^{\text{rd}}$ order polynomial, which describes the dependency well.

The fitted dependency of cS1 on R at the mean value of 100 R slices is displayed in Figure 4.8. Because oscillations are involved with a varying frequency and amplitude, a sine with a 5$^{\text{th}}$ order polynomial for frequency changing and parameters a, b and c for amplitude on the correct cS1 were used:

$$f(x) = (ax + b)\sin(\mathcal{O}(x^5)) + c \tag{4.3}$$

The fit does not match to the first and last period but is good enough for improving the peak shape. A better result would be reachable if a higher order polynomial would be used in the sine.

After the values for the correction functions were determined, the peak shape can be improved. As an example, the peak of ^{222}Rn is used to show the enhancement in Figure 4.9. The Gaussian fit was performed to the uncorrected data, only Z corrected data and R and Z corrected data. The uncorrected peak gives a width of $\sigma = (445.0 \pm 1.2)$ PE and a reduced chi square of $\chi^2_{\text{red}} = 2.00 \pm 0.12$, the Z corrected $\sigma = (433.5 \pm 1.2)$ PE and $\chi^2_{\text{red}} = 1.81 \pm 0.12$ and the R and Z corrected $\sigma = (420.9 \pm 1.1)$ PE and $\chi^2_{\text{red}} = 1.73 \pm 0.12$. Consequential, the corrections lead to a better Gaussian shape and a smaller width which support robust fitting. Now the ccS1 spectrum is prepared to be fitted.

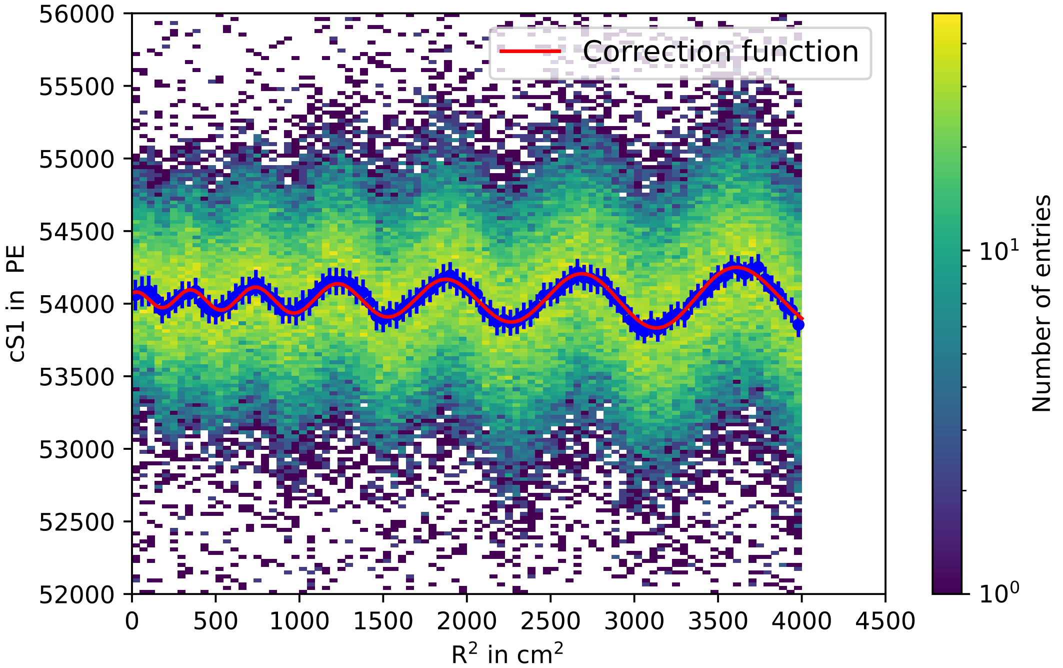

Figure 4.8: cS1/R histogram with the fitted R correction function to the mean cS1 value of the R bins. The fit matches at low and high R^2 not the oscillation perfectly but as good as necessary.

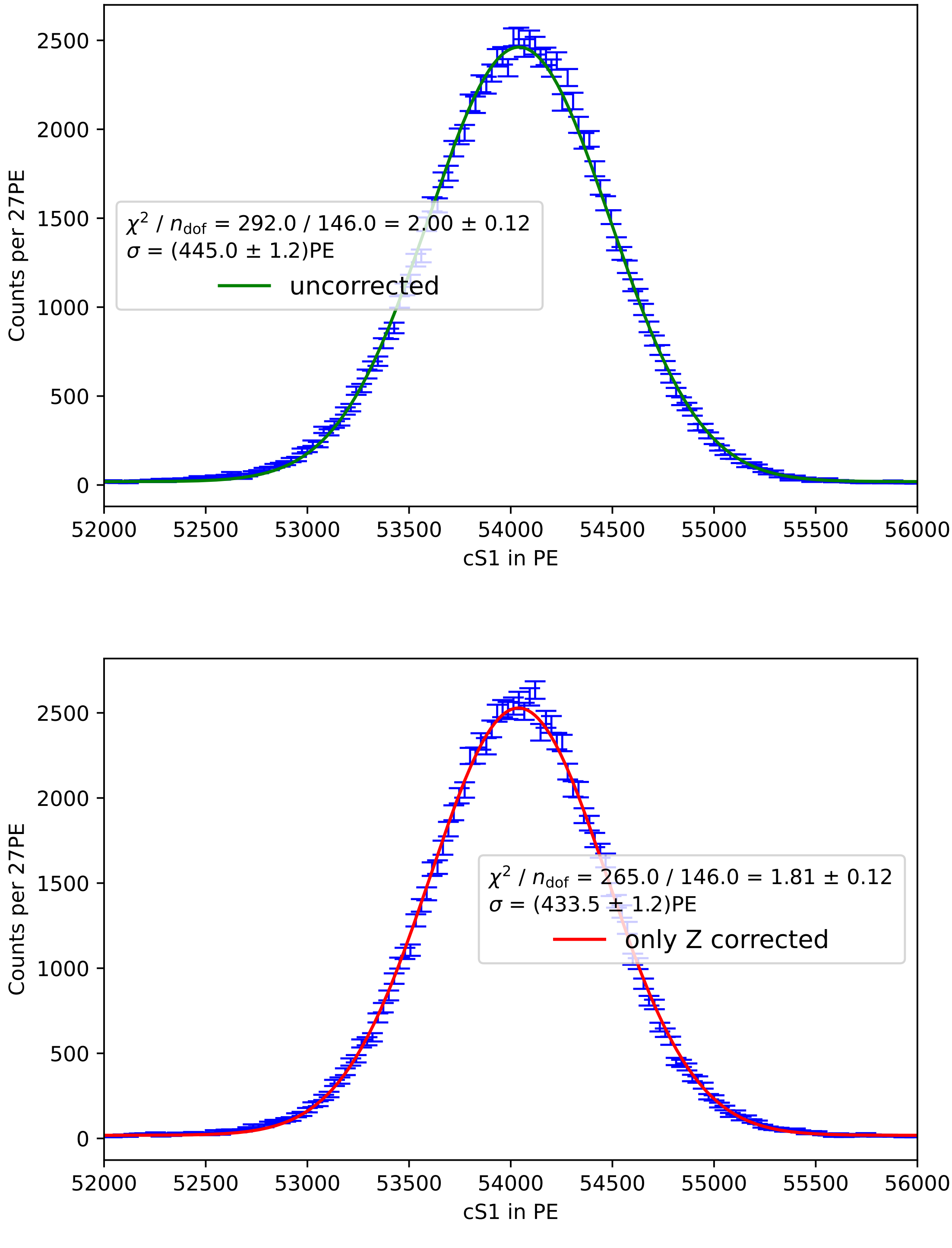

Figure 4.9: (caption on next page)

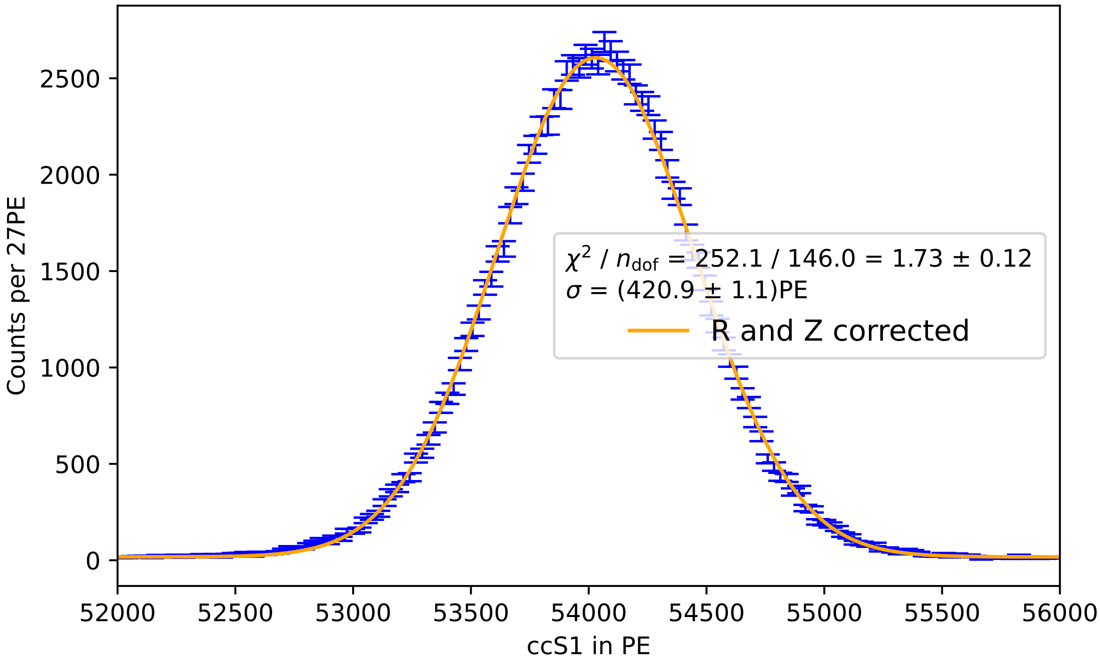

Figure 4.9: Comparison of the ^{222}Rn without own corrections (top), only Z corrected (middle) and R and Z corrected (bottom). The corrections lead to a lower reduced chi square of the Gaussian fit and a peak smaller width.

4.3 Rate evolution

After the preparation of the data, the ccS1 spectrum can be fitted. The goal of a temporal evolution in the activity is reached if the resolution in time is best so the spectra will only have a relatively low event rate. The errors for counts in a binned counting experiment follow a poisson distribution which is approximated as Gaussian errors at high bin counts. But the bin counts in the following spectra will be $n < 10$ beside the α peaks. Therefore, a least squares approach with Gaussian errors can not be applied and a Poisson-likelihood chi-square cost function is used. According to [50] it gives a deviation χ^2 for the n measured values M_i and the predicted values $\mu_i(\theta)$ dependent on the model parameters θ with

$$\chi^2_{\text{Poisson}} = 2\sum_{i=1}^{n}\left(\mu_i(\theta) - M_i + M_i \ln \frac{M_i}{\mu_i(\theta)}\right) \tag{4.4}$$

and for zero count bins it is used

$$\left(\chi^2\right)_{M_i=0} = 2\mu_i(\theta). \tag{4.5}$$

The spectrum model consists of the five involved α decays of ^{222}Rn, ^{218}Po, ^{212}Bi, ^{220}Rn and ^{216}Po with a Gaussian peak contribution and a constant background motivated by the ccS1/cs2 histogram discussed later. Because the light yield varies, the peak positions are set in relation to the disturbance free ^{222}Rn peak. This section will first estimate constraints on the peak position and width of the α peaks also with ^{220}Rn data in the next subsection. After that in subsection 4.3.2, a quick overview over the ^{222}Rn science data will be given. The fitted spectra are discussed in subsection 4.3.3 and the radon reduction is calculated at the end in subsection 4.3.4.

4.3.1 Spectral constraints on ^{220}Rn and daughters

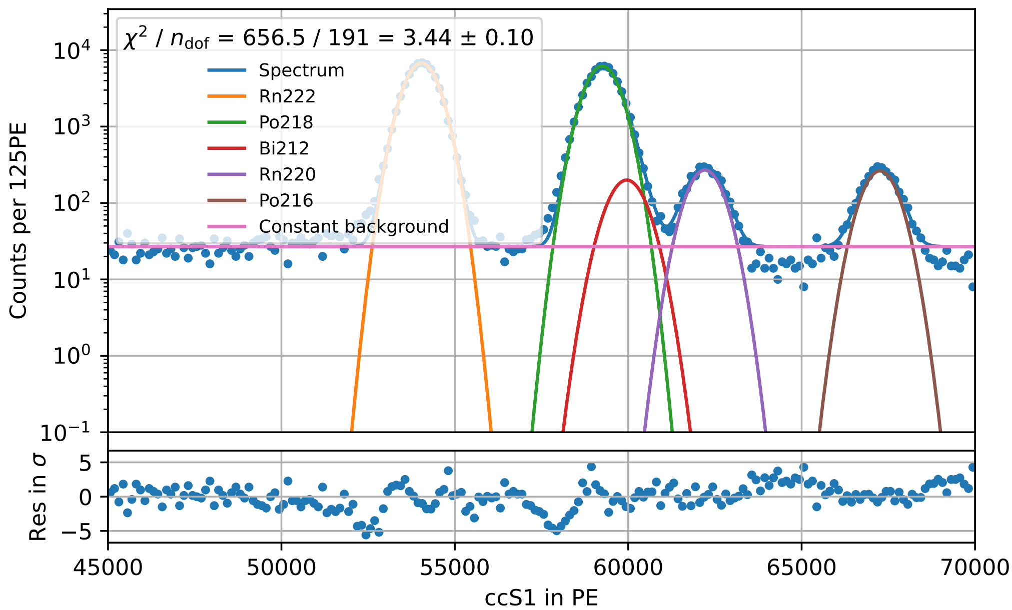

Figure 4.10: ccS1 spectrum of 3 months of science background data for estimating constraints on the α peaks. Huge deviations of the model are at the lower ccS1 flank of the peaks which could originate from a varying light yield. The α peaks except ^{212}Bi can be good observed for setting constraints.

The first constraint is set on ^{220}Rn and ^{216}Po by analyzing most of the science data from 20th August, 2021 in one spectrum where only little ^{212}Bi affects ^{220}Rn and ^{218}Po. The light yield is relatively constant so that the peak positions do not vary critically and thus would broaden the peaks. This complete spectrum is shown in Figure 4.10.

The bad $\chi^2_{\text{red}} = 3.44 \pm 0.10$ is based on the lower ccS1 flank of the peaks and the non constant background where relative high residuals contribute to the χ^2_{red}. This could be connected with a variation of the light yield and the not constant nature of the background source. But as a spectrum for setting constraints on ^{220}Rn and ^{216}Po, their peaks match good enough. One finds for both a likely width of $\sigma \approx 500\,$PE and for ^{222}Rn and ^{218}Po $\sigma \approx 430\,$PE. The positions are ^{222}Rn at 54 kPE, ^{218}Po 1.09× higher, ^{220}Rn 1.15× higher and ^{216}Po 1.24× higher.

In the next step, the ^{220}Rn calibration data is used for setting constraints on ^{212}Bi. The ccS1/cS2 histogram after the S1 AFT cut is displayed in Figure 4.12. At 60 kPE a second population with higher cS2 than the other α decays is observable directly next to the ^{212}Bi population which has the highest activity. The new population could belong to wrongly matched S2s or additional S2s mixed to the originals. In this way it could affect the original correction for the cS1 due to the drift time but in a first order, it is approximately located at the expected ccS1. Beyond this population, the peaks are nearly without any other background.

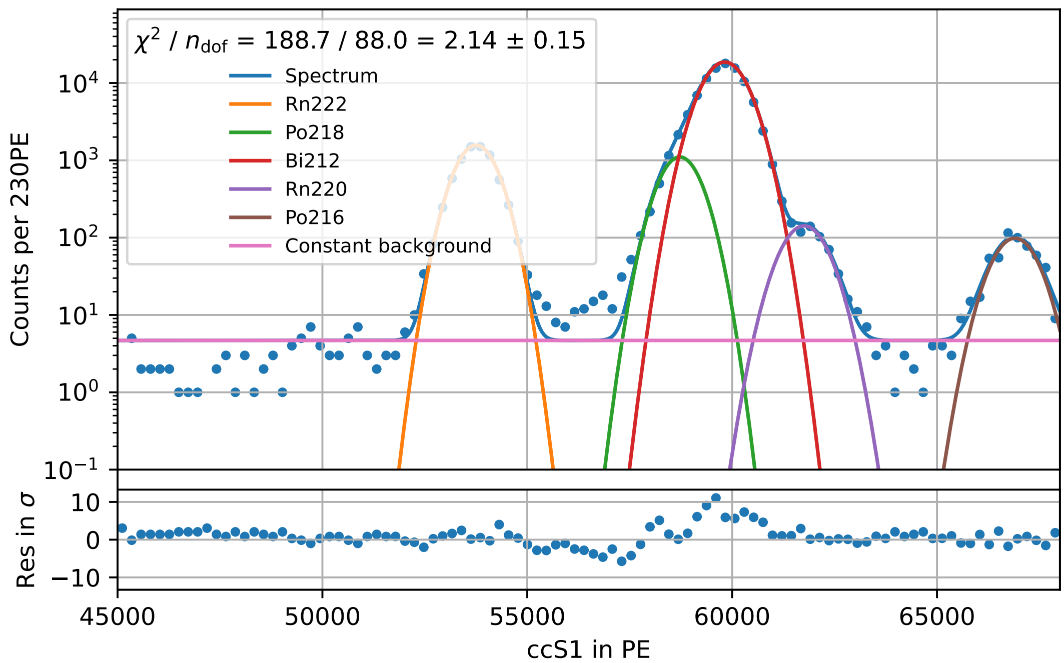

Figure 4.11: Fitted ccS1 spectrum of the ^{220}Rn calibration data for setting constraints on the highest contributing peak of ^{212}Bi.

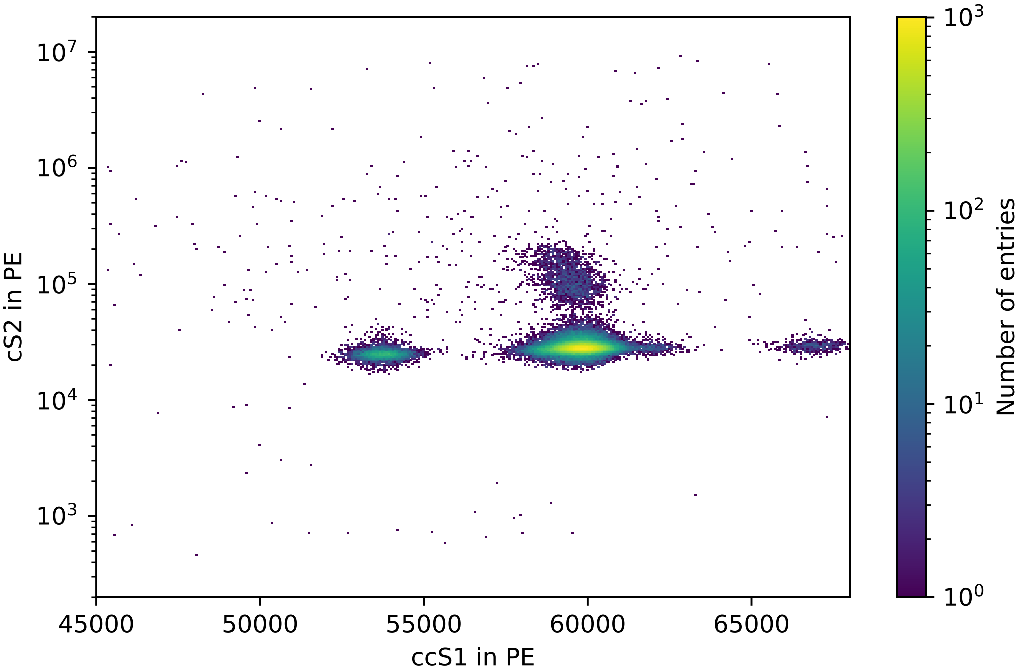

Figure 4.12: ccS1/cs2 histogram of ^{220}Rn data. The α peaks are nearly background free due to the S1 AFT cut. An additional population at 60 kPE and a higher cS2 $= 10^5$ than the other alpha peaks is observable which could belong to wrongly matched S2s.

The fitted ^{220}Rn calibration data ccS1 spectrum is shown in Figure 4.11. It is obvious that ^{212}Bi has the highest activity in the data, although a ^{220}Rn source is used for the calibration and ^{212}Bi only decays with one third by α emission. The reason for that could be the short half-life of ^{220}Rn (55.6 s) so that most of it is already decayed after the induction and more of the longer living product ^{212}Pb (10.64 h) is inserted. However, the high ^{212}Bi activity makes the constraining on it possible. Although the fit converges only at $\chi^2_{\mathrm{red}} = 2.14 \pm 0.15$ and most of the χ^2 is introduced between ^{218}Po and ^{212}Bi, the fit matches the ^{212}Bi peak good enough for an estimation of the width $\sigma \approx 470$ PE and the ccS1 position 1.11× higher than ^{222}Rn.

4.3.2 Data overview

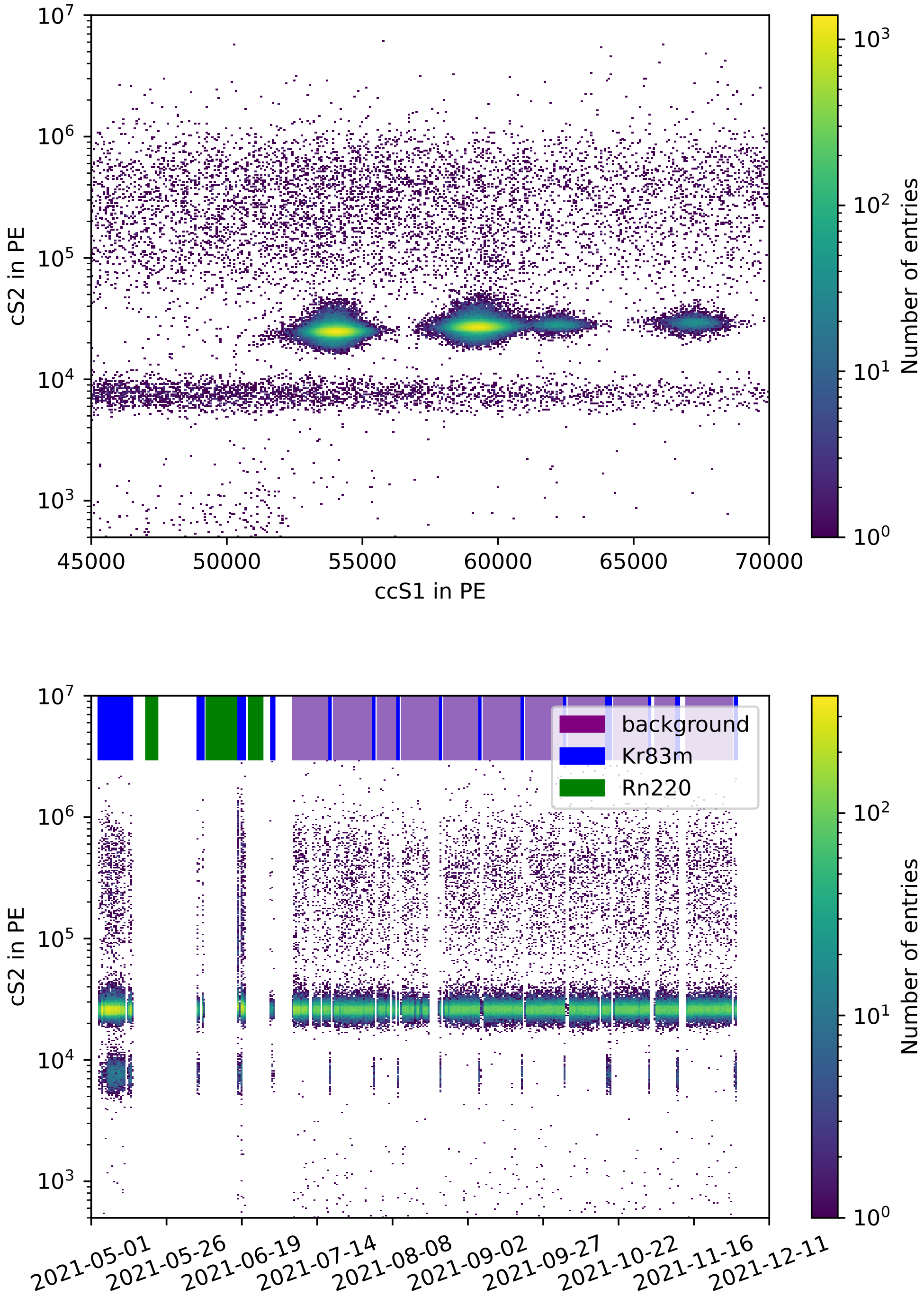

Figure 4.13: Overview of the analyzed data. (Top) The ccS1/cS2 histogram displays clear α populations which are embedded in two slight background bands: The constant one at higher cS2 and a with ccS1 decreasing one at lower cS2. (Bottom) The time/cS2 histogram shows that the origin of the lower cS2 background arises from ^{83m}Kr calibrations and the higher cS2 background is constant over the whole time.

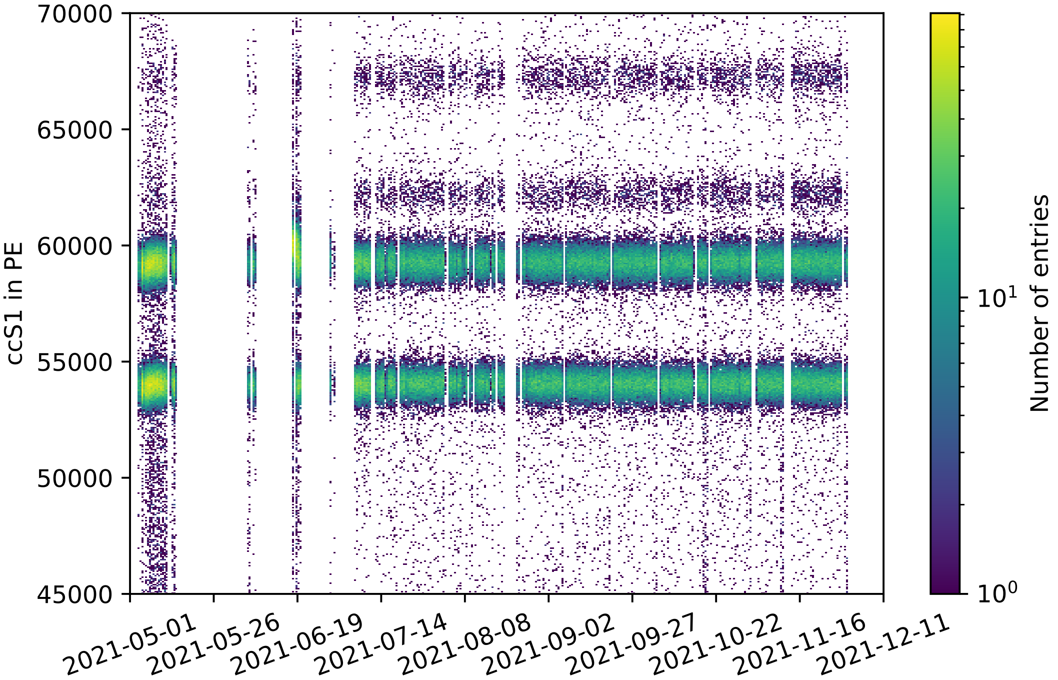

Figure 4.14

Most of the requirements for robust fitting of the spectra is given. As a last step, a further view on the analyzed data is given. Figure 4.13 shows on the top plot the ccS1/cS2 histogram of the whole analyze data. In addition to the α populations, a constant background over the whole ccS1 spectrum with higher cS2 and one with ccS1 decreasing background at lower cS2 are observable. For clarifying the background source, in the bottom plot the cS2 dependent on the time is constructed in a histogram by looking at the different data modes. A direct correlation between the low cS2 background and the $^{83\text{m}}$Kr calibration is obvious so that this background will not contribute most of the time in the spectra. The other background has no time dependence and thus can be added to the spectrum model with a constant coefficient.

The temporal distribution of the ccS1 of the analyze data in Figure 4.14 shows that the ^{220}Rn calibration in June 2021 leaves fragments in the spectrum so that the calculated ^{218}Po rate could be affected. The rest of the used science background data and $^{83\text{m}}$Kr data after July shows a homogeneous distribution and a nearly constant light yield.

4.3.3 α spectrum analysis

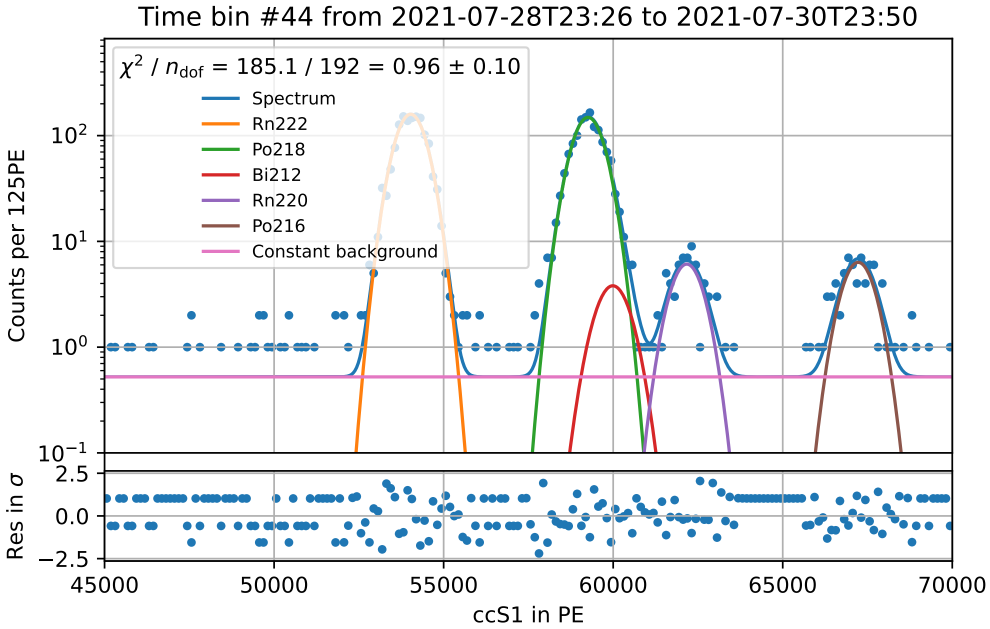

Figure 4.15: Example for a fitted ccS1 spectrum for estimating the radon activity. Looking at the residuals, the model is in a good agreement with the data.

The spectra were fitted by using a time window of ≈ 2 days per spectrum. The peak position and width for every isotope except ^{222}Rn were constrained for a better convergence. Spectra with less detector live time than an hour were left out. An example for a fitted spectrum is shown in Figure 4.15. The $\chi^2_{\mathrm{red}} = 0.96 \pm 0.10$ stays for the good matching fit model. The residuals are homogeneously distributed around 0 except for the area between ^{220}Rn and ^{216}Po where many zero count bins are located. But the important peaks of ^{222}Rn and ^{218}Po are in a good agreement with the fit model so the time range chosen for the bins is not too small.

The χ^2_{red} of all spectrum fits is given in Figure 4.16. Very small values belong to little detector live time during the time window. The high values before June have their reason in the high background and the quickly varying light yield (see Figure 4.14). From August on the desired value of $\chi^2_{\mathrm{red}} = 1$ was mostly not reached because the peaks of ^{220}Rn and ^{216}Po had too less statistics and did not match the model or the unconcerned background after a $^{83\mathrm{m}}$Kr calibration. This background could be added for spectra after a calibration.

The ^{220}Rn background was found to be typically $> 20\times$ lower than ^{222}Rn. This could come from the different concentration of ^{224}Ra and ^{226}Ra and the short half-life of ^{220}Rn (55.6 s) which would lead to a non homogeneous distribution in the whole xenon handling system.

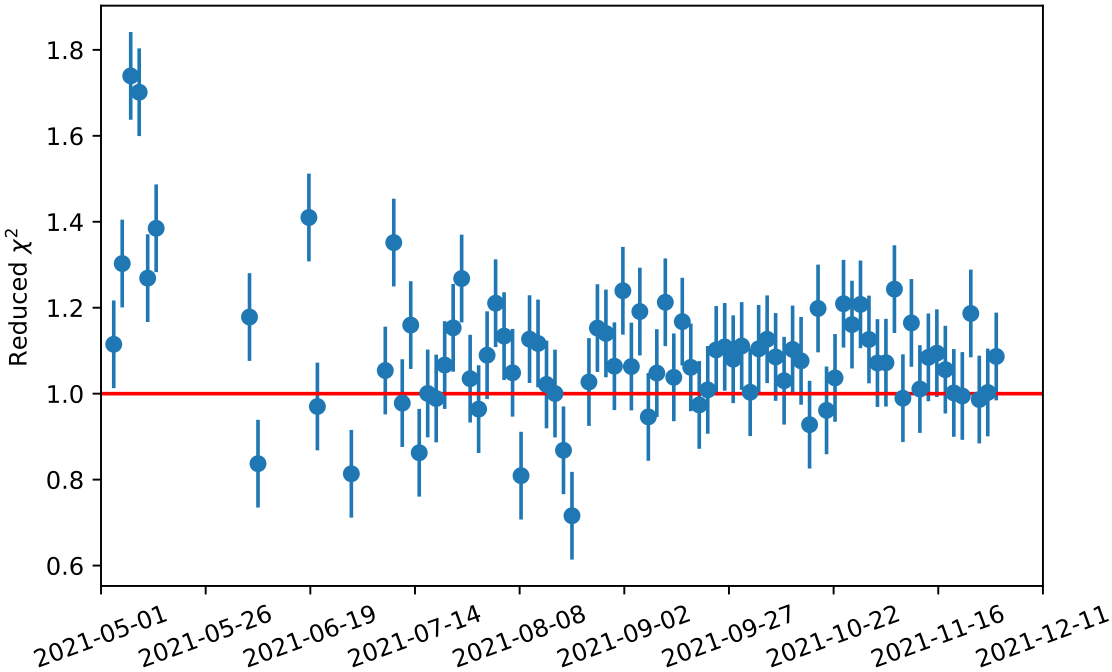

Figure 4.16: χ^2_{red} for the fitted spectra at different times. Huge values at the beginning correlate with higher background and an inconstant light yield. Smaller values than 1 correspond to time bins with lower detector live time. Most of the spectra after July 2021 have $\chi^2_{\text{red}} > 1$ because the fit model matches on the one hand imperfect with low statistic ^{220}Rn and ^{216}Po and on the other the background was only approximated as constant.

4.3.4 Background reduction

As the peak areas are fitted and thus the number of events is known, the rate can be calculated by using the live time via the given detector run times. A correction of this by subtracting the detector dead time has to be done. Therefore, the temporal veto cuts are applied called DAQ (data acquisition) cut and run boundaries cut, which remove all events which were measured only partial. The DAQ veto restricts events which were measured during the DAQ was busy and the run boundaries when the run started or ended. For the whole cut data set of 224728 events, 264 events were restricted by the DAQ veto cut and 122 by the run boundaries cut which had a homogeneously distribution in time. The dead time is supposed as a constant statistical process so that a fraction of 0.17 % live time has to be subtracted. By concerning the the fiducial volume and the density of the xenon, a mass of 4492.1 kg is used for the calculation of the activity per mass.

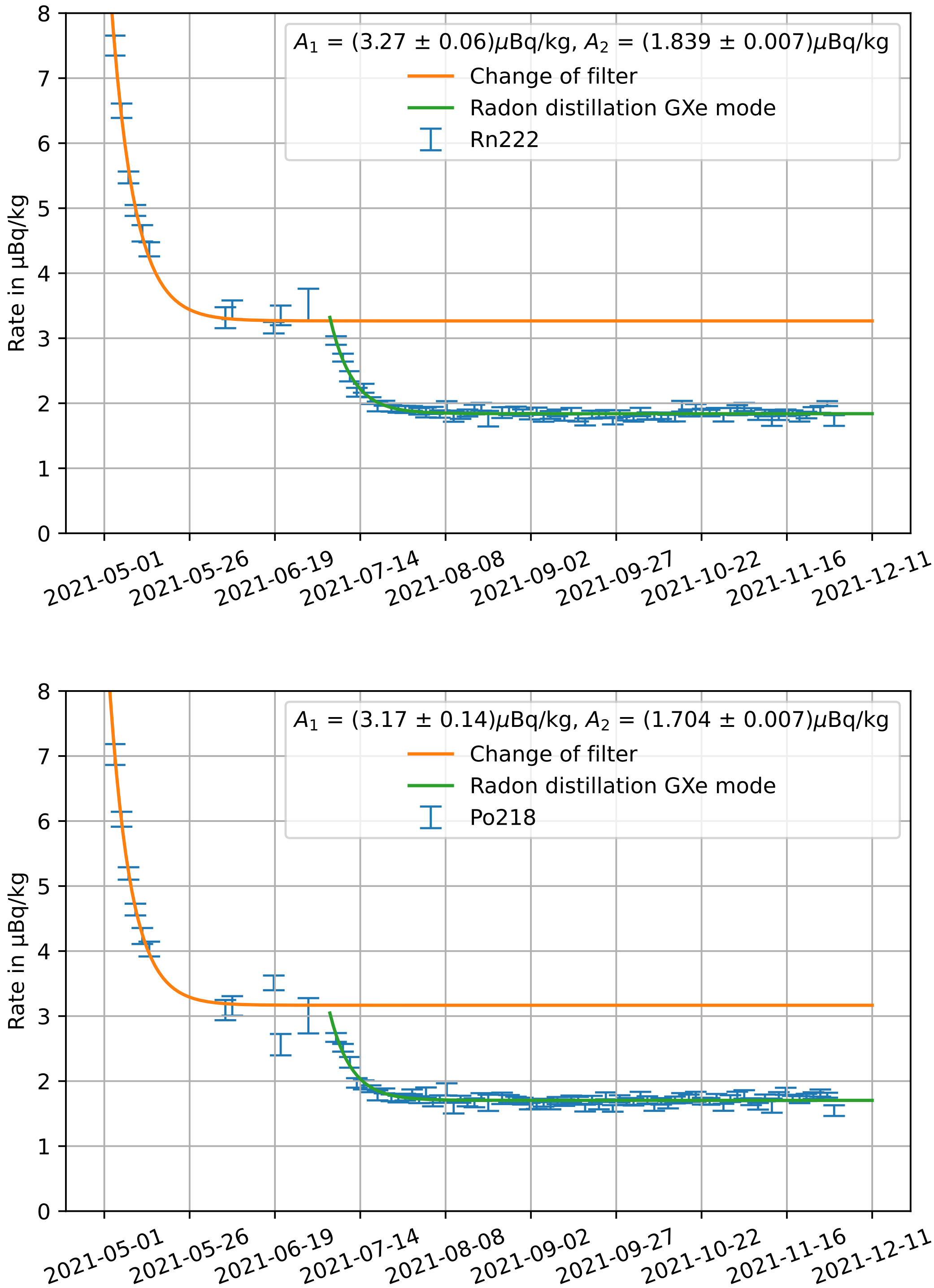

Figure 4.17: Rate evolution of ^{222}Rn (top) and ^{218}Po (bottom) fitted with two exponential decays for changing of filter with lower emanation and the activation of the RRS, respectively. The calculation of the first equilibrium is affected by the low number of bins and the high uncertainties.

The rate evolution of ^{222}Rn (top) and ^{218}Po (bottom) is shown in Figure 4.17. The time values for the rate were chosen as the middle of the time bin so the distribution of the runs within the bin was not concerned which should not affect the final equilibrium which is calculated over several months. During SR0 two operations concerning radon activity were executed: In April 2021, a filter in the LXe purification was changed for lower emanation and the radon removal system was turned on at the beginning of July. For both reductions, an exponential decay was fitted with a least square function to the data.

The fits match all the data whereat the fits before July had too less data for a good estimation about the equilibrium rate.

For ^{222}Rn the activity gets reduced by a factor of 1.78 from $(3.27 \pm 0.06)\,\mu$Bq/kg to $(1.839 \pm 0.007)\,\mu$Bq/kg. The ^{218}Po activity is reduced from $(3.17 \pm 0.14)\,\mu$Bq/kg to $(1.704 \pm 0.007)\,\mu$Bq/kg by factor of 1.86. The 1.08$\times$ lower rate of the ^{218}Po in comparison to the ^{222}Rn despite the low half-life of 3.1 min is explained in [44] with the *cathode cleaning effect*. It is claimed that the fractional ionized isotopes after the α decay drift towards the cathode and get deposited there. For ^{222}Rn, about half of the ^{218}Po atoms are ionized after the decay.

Comparing the activities to the proposed reduction factor of 2 with an initial activity of 4.25 μBq/kg[26], the reduction factor is lower which is based on the here lower initial activity. The published activity value of 1.7 μBq/kg as an upper limit for the ^{214}Pb decay can be reproduced.

5 Conclusion and outlook

Summarizing this thesis, the published ^{222}Rn activity of 1.7 μBq/kg for the first XENONnT science run (SR0) was ratified using the different data analysis approach of less data cuts, using the S1 corrections of the collaboration and minimizing a Poisson-likelihood chi-square function for robust fits at low bin counts.

Chapter 2 introduced the theory for dark matter arising from astronomical observations such as gravitational lenses and galaxy rotation curves. The direct detection of a WIMP as the promising dark matter candidate with xenon dual-phase TPCs was presented as the method with the highest potential. Especially XENONnT with its low background and huge mass of 8.5 t xenon reaches high sensitivities.

The intrinsic backgrounds given as the current problem to overcome and their reduction were discussed in chapter 3. The background of ^{85}Kr was already nearly eliminated whereas ^{136}Xe and ^{124}Xe as a high energy background are hard to reduce. The main low energy background for the WIMP search is induced by ^{214}Pb coming from emanated ^{222}Rn. The detector components have already been changed to low radioactive materials but a further decrease of the low ^{222}Rn activity of 4.2 μBq/kg can be reached by the novel online cryogenic radon removal system. A modified McCabe-Thiele distillation concept is used, where the contaminant ^{222}Rn decays within the distillation column and thus no extraction, connected with xenon loss, is needed. The cooling concept combined with a Claudius-Rankine cycle features a connection of the needed cooling and heating power and therefore reduces the required cooling power with liquid nitrogen from 3 kW to 1 kW. The GXe and LXe mode both should reduce the ^{222}Rn activity by a factor of 2, respectively, while acting with a flow of > 71 kg/h (200 slpm) so that the goal of 1 μBq/kg can be archived. This reduction can be proofed by doing an α spectrum analysis which sets an upper limit to the ^{214}Pb activity by estimating the ^{218}Po activity via a Gaussian S1 peak fitting.

This α analysis was performed in chapter 4 by preparing the data with cuts and corrections and setting constraints on the peaks. A fiducialization on the spatial parameters could reject many backgrounds by using the self-shielding of the xenon whereby backgrounds were rejected arising from the wall, the gas or falsely corrected events in the inhomogeneous field areas of the TPC. High energy correction deficits were revised by applying own corrections in Z and R which led to a better Gaussian-like peak shape. The problematic area around the ^{218}Po peak affected by decays of ^{220}Rn and ^{212}Bi was well understood by investigating peak position and width constraints from high statistic background data and ^{220}Rn calibration data. By using these constraints, the temporal rate evolution for ^{222}Rn and ^{218}Po could be calculated by robust fitting via a Poisson-likelihood chi-square function despite the low statistics of only 2 d per spectrum. The equilibrium activity at the end of SR0 is for ^{222}Rn $(1.839 \pm 0.007)\,\mu$Bq/kg and for ^{218}Po $(1.704 \pm 0.007)\,\mu$Bq/kg, which supports the published value and the radon depletion by the RRS in GXe mode only.

As an outlook, XENONnT currently takes data for the next science run with the RRS in the LXe and GXe mode and hence a ^{222}Rn activity of $< 1\,\mu$Bq/kg. Lower activities should be reachable for higher flows and larger cooling and heating power within the distillation column. A higher sensitivity for the WIMP search with longer data taking than SR0 will set new limits on the WIMP cross section and maybe one day proof the existence of dark matter.

Appendix

Fit parameters for the corrections

Using for the Z correction

$$f(x) = a + b(x - x_0) + c(x - x_0)^2 + d(x - x_0)^3 \tag{5.1}$$

and for the R correction

$$f(x) = (ax + b)\sin(\mathcal{O}(x^5)) + c \tag{5.2}$$

$$\mathcal{O}(x^5) = d + ex + fx^2 + gx^3 + hx^4 + ix^5 \tag{5.3}$$

the fit parameters are

	Z correction	R correction
x_0	(-110 ± 50)	/
a	(53880 ± 190)	$(4.7 \pm 1.4)10^{-2}$
b	(4.0 ± 1.7)	(49 ± 27)
c	(0.02 ± 0.05)	(54030 ± 9)
d	$(-32 \pm 7)10^{-5}$	(1.1 ± 0.9)
e	/	$(2.14 \pm 0.14)10^{-2}$
f	/	$(-52 \pm 6)10^{-7}$
g	/	$(37 \pm 9)10^{-11}$
h	/	$(169.1 \pm 2.8)10^{-15}$
i	/	$(3 \pm 240)10^{-17}$

Bibliography

[1] M. Persic, P. Salucci, and F. Stel, "The universal rotation curve of spiral galaxies—I. The dark matter connection," *Monthly Notices of the Royal Astronomical Society*, vol. 281, no. 1, pp. 27–47, 1996.

[2] E. Corbelli and P. Salucci, "The extended rotation curve and the dark matter halo of M33," *Monthly Notices of the Royal Astronomical Society*, vol. 311, no. 2, pp. 441–447, 2000.

[3] P. Salucci, A. Lapi, C. Tonini, G. Gentile, I. Yegorova, and U. Klein, "The universal rotation curve of spiral galaxies–II. The dark matter distribution out to the virial radius," *Monthly Notices of the Royal Astronomical Society*, vol. 378, no. 1, pp. 41–47, 2007.

[4] N. Kaiser and G. Squires, "Mapping the dark matter with weak gravitational lensing," *The Astrophysical Journal*, vol. 404, pp. 441–450, 1993.

[5] S. Dodelson and L. M. Widrow, "Sterile neutrinos as dark matter," *Physical Review Letters*, vol. 72, no. 1, p. 17, 1994.

[6] U. Seljak, A. Makarov, P. McDonald, and H. Trac, "Can sterile neutrinos be the dark matter?" *Physical Review Letters*, vol. 97, no. 19, p. 191 303, 2006.

[7] A. Boyarsky, M. Drewes, T. Lasserre, S. Mertens, and O. Ruchayskiy, "Sterile neutrino dark matter," *Progress in Particle and Nuclear Physics*, vol. 104, pp. 1–45, 2019.

[8] L. D. Duffy and K. Van Bibber, "Axions as dark matter particles," *New Journal of Physics*, vol. 11, no. 10, p. 105 008, 2009.

[9] P. Sikivie, "Dark matter axions," *International Journal of Modern Physics A*, vol. 25, no. 02n03, pp. 554–563, 2010.

[10] M. Pospelov, A. Ritz, and M. Voloshin, "Secluded WIMP dark matter," *Physics Letters B*, vol. 662, no. 1, pp. 53–61, 2008.

[11] L. Roszkowski, E. M. Sessolo, and S. Trojanowski, "WIMP dark matter candidates and searches—current status and future prospects," *Reports on Progress in Physics*, vol. 81, no. 6, p. 066 201, 2018.

[12] E. Aprile and T. Doke, "Liquid xenon detectors for particle physics and astrophysics," *Reviews of Modern Physics*, vol. 82, no. 3, p. 2053, 2010.

[13] R. Bernabei *et al.*, "New limits on particle dark matter search with a liquid Xenon target-scintillator," *Physics Letters B*, vol. 436, no. 3-4, pp. 379–388, 1998.

[14] X. Cao *et al.*, "PandaX: a liquid xenon dark matter experiment at CJPL," *Science China Physics, Mechanics & Astronomy*, vol. 57, no. 8, pp. 1476–1494, 2014.

[15] E. Aprile *et al.*, "The XENON100 dark matter experiment," *Astroparticle Physics*, vol. 35, no. 9, pp. 573–590, 2012.

[16] D. Akerib *et al.*, "The large underground xenon (LUX) experiment," *Nuclear Instruments and Methods in Physics Research Section A: Accelerators, Spectrometers, Detectors and Associated Equipment*, vol. 704, pp. 111–126, 2013.

[17] E. Aprile *et al.*, "The XENON1T dark matter experiment," *The European Physical Journal C*, vol. 77, no. 12, pp. 1–23, 2017.

[18] E. Aprile *et al.*, "Projected WIMP sensitivity of the XENONnT dark matter experiment," *Journal of Cosmology and Astroparticle Physics*, vol. 2020, no. 11, p. 031, 2020.

[19] E. Aprile *et al.*, "First dark matter search results from the XENON1T experiment," *Physical review letters*, vol. 119, no. 18, p. 181 301, 2017.

[20] E. Aprile *et al.*, "Search for new physics in electronic recoil data from XENONnT," *Physical Review Letters*, vol. 129, no. 16, p. 161 805, 2022.

[21] "Observation of two-neutrino double electron capture in ^{124}Xe with XENON1T," *Nature*, vol. 568, no. 7753, pp. 532–535, 2019.

[22] E. Aprile *et al.*, " ^{222}Rn emanation measurements for the XENON1T experiment," *The European Physical Journal C*, vol. 81, no. 4, pp. 1–14, 2021.

[23] E. Aprile *et al.*, "Material radiopurity control in the XENONnT experiment," *arXiv preprint arXiv:2112.05629*, 2021.

[24] E. Aprile *et al.*, "Online ^{222}Rn removal by cryogenic distillation in the XENON100 experiment," *The European Physical Journal C*, vol. 77, no. 6, pp. 1–8, 2017.

[25] S. Brünner, "Mitigation of ^{222}Rn induced background in the XENON1T dark matter experiment," Combined Faculties of the Natural Sciences and Mathematics of the Ruperto-Carola University of Heidelberg, 2017.

[26] M. Murra, D. Schulte, C. Huhmann, and C. Weinheimer, "Design, construction and commissioning of a high-flow radon removal system for XENONnT," *arXiv preprint arXiv:2205.11492*, 2022.

[27] C. S. Frenk and S. D. White, "Dark matter and cosmic structure," *Annalen der Physik*, vol. 524, no. 9-10, pp. 507–534, 2012.

[28] J.-H. He, B. Wang, and P. Zhang, "Imprint of the interaction between dark sectors in large scale cosmic microwave background anisotropies," *Physical Review D*, vol. 80, no. 6, p. 063 530, 2009.

[29] F. Jörg, “From ^{222}Rn measurements in XENONnT and HeXe to radon mitigation in future liquid xenon experiments,” Combined Faculties of the Natural Sciences and Mathematics of the Ruperto-Carola University of Heidelberg, 2022.

[30] “Image of ESA/Hubble.” (Dec. 4, 2022), [Online]. Available: `https://esahubble.org/images/heic1106c/`.

[31] A. Bolozdynya, “Two-phase emission detectors and their applications,” *Nuclear Instruments and Methods in Physics Research Section A: Accelerators, Spectrometers, Detectors and Associated Equipment*, vol. 422, no. 1-3, pp. 314–320, 1999.

[32] L. Althüser, “Light collection efficiency simulations of the XENON1T experiment and comparison to data,” Master’s thesis, WWU Münster, 2017.

[33] G. Alner *et al.*, “First limits on WIMP nuclear recoil signals in ZEPLIN-II: A two-phase xenon detector for dark matter detection,” *Astroparticle Physics*, vol. 28, no. 3, pp. 287–302, 2007.

[34] D. Akerib *et al.*, “Discrimination of electronic recoils from nuclear recoils in two-phase xenon time projection chambers,” *Physical Review D*, vol. 102, no. 11, p. 112 002, 2020.

[35] E. Aprile *et al.*, “Conceptual design and simulation of a water Cherenkov muon veto for the XENON1T experiment,” *Journal of instrumentation*, vol. 9, no. 11, P11006, 2014.

[36] E. Aprile *et al.*, “Removing krypton from xenon by cryogenic distillation to the ppq level,” *The European Physical Journal C*, vol. 77, no. 5, pp. 1–12, 2017.

[37] P. Linstorm, “NIST chemistry webbook, NIST standard reference database number 69,” *J. Phys. Chem. Ref. Data, Monograph*, vol. 9, 1998.

[38] E. Aprile, X. Collaboration, *et al.* “Suplemental data for material radiopurity control in the XENONnT experiment. Zenodo repository (2021).” (Dec. 13, 2022), [Online]. Available: `https://doi.org/10.5281/zenodo.5767293`.

[39] G. Zuzel and H. Simgen, “High sensitivity radon emanation measurements,” *Applied Radiation and Isotopes*, vol. 67, no. 5, pp. 889–893, 2009.

[40] N. Rupp, “On the detection of ^{222}Rn with miniaturized proportional counters: background, sensitivity studies and results for XENON1T,” Ph.D. dissertation, Ruprecht-Karls-Universität Heidelberg, 2015.

[41] S. Bruenner, D. Cichon, S. Lindemann, T. M. Undagoitia, and H. Simgen, “Radon depletion in xenon boil-off gas,” *The European Physical Journal C*, vol. 77, no. 3, pp. 1–6, 2017.

[42] *Sulzer Chemtech Ltd, Structured packings: energy-efficient, innovative and profitable*, version 22.13.06.40 V.15, 2015.

[43] D. Schulte, M. Murra, P. Schulte, C. Huhmann, and C. Weinheimer, “Ultra-clean radon-free four cylinder magnetically-coupled piston pump,” *Journal of Instrumentation*, vol. 16, no. 09, P09011, 2021.

[44] P. A. Breur, “Backgrounds in XENON1T,” Ph.D. dissertation, NARCIS, 2019.

[45] E. Aprile, X. Collaboration, *et al.* “The straxen data processor v1.7.2.” (2022), [Online]. Available: `https://doi.org/10.5281/zenodo.6553131`.

[46] L. Kastens, S. Cahn, A. Manzur, and D. McKinsey, “Calibration of a liquid xenon detector with ^{83m}Kr,” *Physical Review C*, vol. 80, no. 4, p. 045 809, 2009.

[47] S. Baker and R. D. Cousins, “Clarification of the use of chi-square and likelihood functions in fits to histograms,” *Nuclear Instruments and Methods in Physics Research*, vol. 221, no. 2, pp. 437–442, 1984.

[48] H. Dembinski and P. O. et al., “scikit-hep/iminuit,” DOI: `10.5281/zenodo.3949207`. [Online]. Available: `https://doi.org/10.5281/zenodo.3949207`.

[49] N. M. R. E. Rupp, “Radon induced background in the XENON1T dark matter search experiment and studies on xenon purity in the HeXe system,” Combined Faculties of the Natural Sciences and Mathematics of the Ruperto-Carola University of Heidelberg, 2020.

[50] X. Ji, W. Gu, X. Qian, H. Wei, and C. Zhang, “Combined Neyman–Pearson chi-square: An improved approximation to the Poisson-likelihood chi-square,” *Nuclear Instruments and Methods in Physics Research Section A: Accelerators, Spectrometers, Detectors and Associated Equipment*, vol. 961, p. 163 677, 2020.